Langtaosha (LTS) Preprint doi: https://doi.org/10.65215/LTSpreprints.2026.11.14.000388. This version posted November 14, 2026. The copyright holder for this preprint (which was not certified by peer review) is the author/funder. Creative Commons license: CC Attribution-NonCommercial-NoDerivatives 4.0 https://creativecommons.org/licenses/by-nc-nd/4.0

Covalent flavin installation enables peptide-scale proximity proteomics of microproteins in living cells

Zuye Fang[1], Chaohong Bao[1,2], Yide He[3], Xinyu Zhang[1,4], Min Guo[1], Kejia Li[1], Xi Yang[1], Lin Deng[3], Gang Li[1*]

[1]Institute of Chemical Biology, Shenzhen Bay Laboratory, Shenzhen 518132, China

[2]State Key Laboratory of Crop Stress Biology for Arid Areas, College of Life Sciences, Northwest A & F University, Yangling 712100 China

[3]Institute of Molecular Physiology, Shenzhen Bay Laboratory, Shenzhen 518132, China

[4]Shenzhen Medical Academy of Research and Translation, Shenzhen, 518107, China

*Correspondence: ligang@szbl.ac.cn

ABSTRACT

Microproteins often derive their functions from context-dependent molecular interactions, yet their small size makes proximity mapping particularly susceptible to perturbation by protein-sized labeling enzymes. Here we develop flavin-mediated peptide-tag proximity labeling (FPPL), which decouples photocatalyst installation from the protein of interest. In FPPL, ApbE covalently installs FMN onto a 12-amino-acid ApbE acceptor peptide (AAP) fused to the target protein, generating a light-responsive photocatalytic center in living cells. AAP fusion largely preserved the localization of microprotein NUPR1 and BANF1 compared with direct TurboID fusion, while supporting spatially selective proteome mapping across distinct subcellular compartments. Applying FPPL to BANF1 revealed a functionally connected nuclear homeostatic network, as depletion of multiple

Langtaosha (LTS) Preprint doi: https://doi.org/10.65215/LTSpreprints.2026.11.14.000388. This version posted November 14, 2026. The copyright holder for this preprint (which was not certified by peer review) is the author/funder. Creative Commons license: CC Attribution-NonCommercial-NoDerivatives 4.0 https://creativecommons.org/licenses/by-nc-nd/4.0

FPPL-identified proteins induced nuclear reporter leakage, focal BANF1 recruitment and local lamina remodeling. FPPL profiling of GNG4 unexpectedly uncovered a virus-associated proximal network and identified GNG4 as a positive regulator of Sendai-virus-induced *IFNB1* expression and downstream STAT1 signaling. Several GNG4-proximal proteins further modulated this response, with ARF6 and MTCH2 partially restoring antiviral signaling in GNG4-depleted cells. Together, FPPL establishes enzymatic covalent flavin installation as a distinct architecture for peptide-scale proximity proteomics and enables minimally perturbative discovery of functional microprotein networks in living cells.

INTRODUCTION

Microproteins, broadly defined as proteins of approximately 100 amino acids or fewer, are increasingly recognized as a functionally important component of the proteome[1-3]. Ribosome profiling and proteogenomic analyses have substantially expanded the catalogue of translated short open reading frames[4,5], while functional studies have revealed roles for individual microproteins in metabolism, stress responses, membrane dynamics and immunity[6-13]. Many of these functions are mediated through specific molecular interactions. For example, the 34-amino-acid DWORF regulates the SERCA calcium pump[14,15], the 56-amino-acid mitoregulin influences mitochondrial respiratory organization and metabolism[16], and the 84-amino-acid myomixer cooperates with myomaker to promote myoblast fusion[17]. These studies highlight molecular interactions as an important route to understanding microprotein function[18]. However, many translated short open reading frames remain functionally unassigned[3,19,20], and experimental approaches that substantially perturb these small proteins may obscure their native localization, molecular interactions and function.

Langtaosha (LTS) Preprint doi: https://doi.org/10.65215/LTSpreprints.2026.11.14.000388. This version posted November 14, 2026. The copyright holder for this preprint (which was not certified by peer review) is the author/funder. Creative Commons license: CC Attribution-NonCommercial-NoDerivatives 4.0 https://creativecommons.org/licenses/by-nc-nd/4.0

Mapping the molecular environments of microproteins remains technically challenging. Affinity purification and co-immunoprecipitation can fail to preserve weak, transient or membrane-associated interactions, whereas proximity labeling approaches record the local protein environment in living cells without requiring molecular complexes to remain intact during lysis[21-26]. Proximity labeling has been applied to microprotein interaction mapping using APEX/APEX2 and, more recently, TurboID, enabling the identification of interaction partners for microproteins including CYREN, C11orf98, MIEF1-MP and FAM229B[27-29]. However, these approaches require direct fusion of a protein-sized catalytic enzyme to the microprotein. For microproteins, such fusions can represent a substantial structural addition and may alter localization, sterically interfere with molecular contacts or otherwise perturb native behavior[30,31]. A central challenge is therefore to position labeling activity at a microprotein while minimizing the genetically encoded component directly attached to it.

We reasoned that this challenge could be addressed by separating photocatalyst installation from the protein of interest. The bacterial flavin transferase ApbE catalyzes covalent transfer of an FMN group from FAD to an acceptor threonine within a defined peptide sequence[32,33]. A 12-amino-acid ApbE acceptor peptide (AAP; GVDGLSGATLTS) have been developed to enable site-specific covalent flavinylation by ApbE, with subsequent studies improving flavin incorporation efficiency and expanding the range of transferable flavin cofactors[34-36]. Importantly, ApbE-mediated covalent FMN modification has also been demonstrated in living mammalian cells[37]. Previous studies have demonstrated that flavin-containing photosensitizers can mediate light-dependent protein labeling in biological environments[38-41]. We therefore envisioned that ApbE supplied in trans could install a photocatalytic cofactor directly onto AAP fused to the protein of interest. This architecture decouples the protein-sized cofactor-installing enzyme from

Langtaosha (LTS) Preprint doi: https://doi.org/10.65215/LTSpreprints.2026.11.14.000388. This version posted November 14, 2026. The copyright holder for this preprint (which was not certified by peer review) is the author/funder. Creative Commons license: CC Attribution-NonCommercial-NoDerivatives 4.0 https://creativecommons.org/licenses/by-nc-nd/4.0

the target while positioning the photocatalyst directly on a peptide-scale targeting element. Unlike ASAP-ID, which uses short peptide epitopes to recruit antibody-linked labeling enzymes[42], FPPL does not require persistent recruitment of a protein-sized catalyst to the target. FPPL also differs from compact enzyme-fusion approaches such as ultraID[43], which reduce the size of the labeling enzyme but still rely on a protein-based catalyst directly fused to the target.

Here we establish flavin-mediated peptide-tag proximity labeling (FPPL), in which ApbE covalently installs FMN onto AAP to enable blue-light-dependent labeling of nearby proteins in living cells. AAP fusion largely preserves the localization of the microproteins NUPR1 and BANF1 compared with direct TurboID fusion, while supporting spatially selective proteome mapping across distinct subcellular compartments. Application of FPPL to BANF1 reveals a functionally connected protein network involved in nuclear-envelope integrity, with depletion of multiple FPPL-identified proteins promoting nuclear reporter leakage, focal BANF1 recruitment and local lamina remodeling. FPPL profiling of GNG4 further uncovers an unexpected virus-associated proximal network and identifies GNG4 as a positive regulator of Sendai-virus-induced *IFNB1* expression and downstream STAT1 signaling. Together, these findings establish enzymatic covalent flavin installation as a distinct design principle for peptide-scale proximity proteomics of microproteins and link their local molecular environments to cellular function.

RESULTS

Decoupling catalyst installation from the target enables peptide-scale proximity labeling. Most proximity-labeling methods require direct fusion of a catalytic enzyme to the protein of interest (POI). Although such fusions are compatible with many proteins, they can represent a substantial structural addition to microproteins and may alter their localization or accessibility to

Langtaosha (LTS) Preprint doi: https://doi.org/10.65215/LTSpreprints.2026.11.14.000388. This version posted November 14, 2026. The copyright holder for this preprint (which was not certified by peer review) is the author/funder. Creative Commons license: CC Attribution-NonCommercial-NoDerivatives 4.0 https://creativecommons.org/licenses/by-nc-nd/4.0

molecular partners (Fig. 1A). We therefore sought to minimize the genetically encoded component attached to the POI while retaining labeling activity in its immediate molecular environment.

The bacterial flavin transferase ApbE catalyzes covalent transfer of FMN from FAD to a short peptide substrate. We used the AAP as a peptide-scale fusion and first asked whether reducing the fusion size could lessen perturbation of microproteins. We selected NUPR1, an 82-amino-acid stress-responsive nuclear protein involved in transcriptional regulation and cellular adaptation to stress[44,45], as an initial model. Previous studies have demonstrated that NUPR1 predominantly localizes to the nucleus under proliferative conditions and undergoes regulated nuclear translocation mediated by its nuclear localization signal[45-47]. Consistent with these findings, NUPR1 displayed predominantly nuclear localization, which was largely retained by NUPR1-AAP (Fig. 1B). By contrast, NUPR1-TurboID displayed more prominent extranuclear localization. Fluorescence intensity profiling across individual cells showed close correspondence between the Flag and Hoechst signals for NUPR1 and NUPR1-AAP, whereas the NUPR1-TurboID signal extended beyond the nuclear boundary (Fig. 1C). Consistently, the nuclear-to-cytoplasmic fluorescence ratio was similar between NUPR1 and NUPR1-AAP but markedly reduced for NUPR1-TurboID (Fig. 1D). We next examined BANF1, an 89-amino-acid DNA-binding protein with established roles in chromatin organization, nuclear-envelope assembly and repair[48,49]. Consistent with these nuclear functions, the OpenCell proteome-scale localization atlas identifies BANF1 in nuclear compartments, including the nucleoplasm, chromatin and nuclear membrane[50]. In agreement with this localization profile, BANF1-AAP largely retained the nuclear distribution of BANF1, whereas BANF1-TurboID exhibited greater extranuclear localization (Supplementary Fig. 1). Thus, for both compact proteins examined, fusion to AAP was associated with less apparent localization perturbation than direct fusion to TurboID.

Langtaosha (LTS) Preprint doi: https://doi.org/10.65215/LTSpreprints.2026.11.14.000388. This version posted November 14, 2026. The copyright holder for this preprint (which was not certified by peer review) is the author/funder. Creative Commons license: CC Attribution-NonCommercial-NoDerivatives 4.0 https://creativecommons.org/licenses/by-nc-nd/4.0

These observations motivated a proximity labeling architecture in which the protein-sized cofactor-installing enzyme is physically separated from the POI. We therefore developed flavin-mediated peptide-tag proximity labeling (FPPL; Fig. 1E). In FPPL, the POI is fused only to AAP, whereas ApbE is expressed separately and covalently installs FMN onto the peptide. We reasoned that blue-light excitation of the protein-tethered flavin, in the presence of an alkyne-containing probe, could drive local chemical labeling of proteins surrounding the POI. Probe-labeled proteins could subsequently be conjugated to azide-biotin by click chemistry, enriched and identified by LC-MS/MS. FPPL therefore decouples the protein-sized cofactor-installing enzyme from the target while positioning the photocatalytic cofactor directly on a peptide-scale targeting element.

Langtaosha (LTS) Preprint doi: https://doi.org/10.65215/LTSpreprints.2026.11.14.000388. This version posted November 14, 2026. The copyright holder for this preprint (which was not certified by peer review) is the author/funder. Creative Commons license: CC Attribution-NonCommercial-NoDerivatives 4.0 https://creativecommons.org/licenses/by-nc-nd/4.0

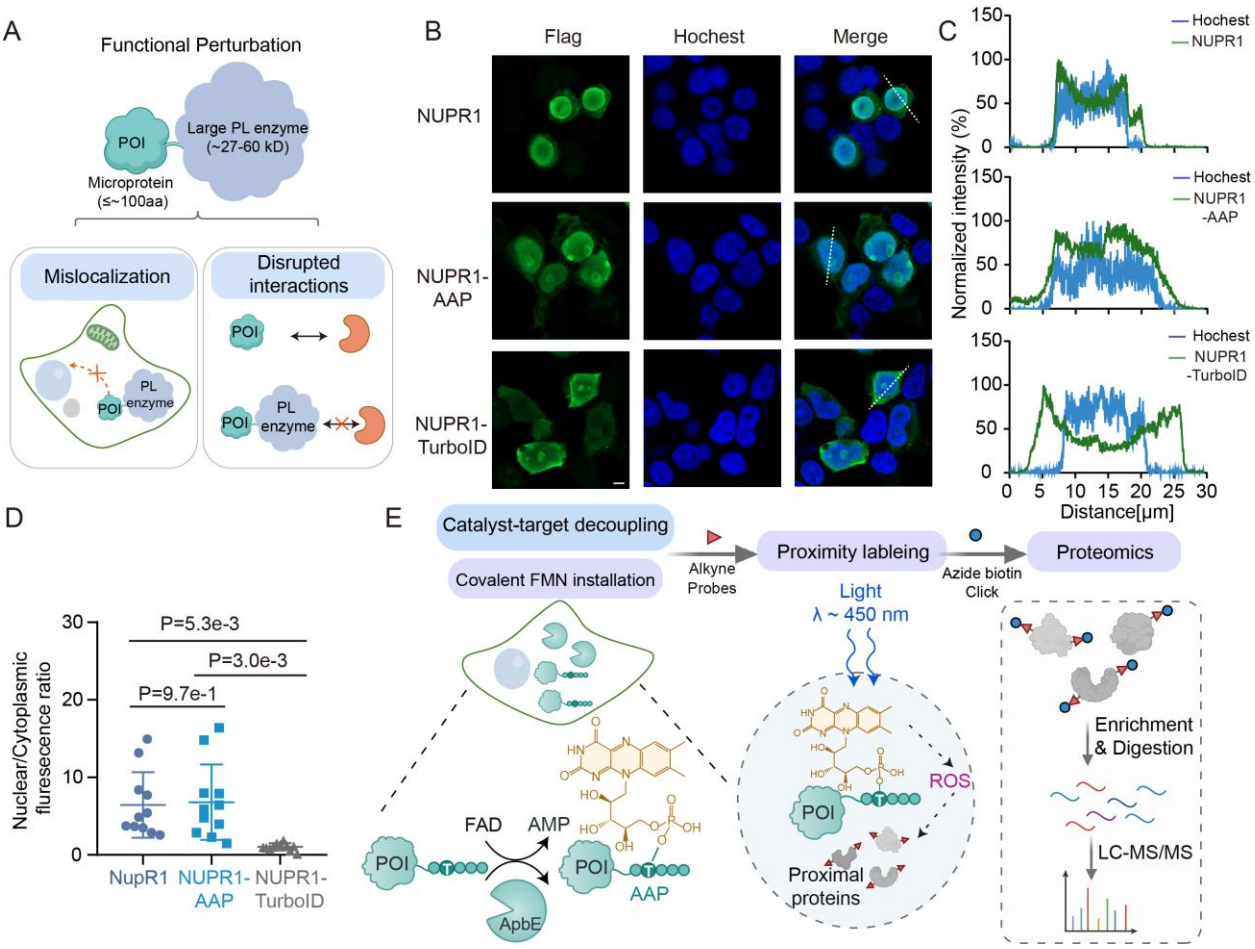


Fig. 1 Design of FPPL for minimally perturbative proximity labeling of microproteins. A) Schematic illustrating the potential perturbation caused by direct fusion of a protein-sized proximity-labeling (PL) enzyme (~27–60 kDa) to a microprotein. Such fusions may alter the subcellular localization of the protein of interest (POI) or interfere with its native molecular interactions. **B**) Representative immunofluorescence images of cells expressing Flag-tagged NUPR1, NUPR1-AAP or NUPR1-TurboID. Flag immunofluorescence is shown in green and Hoechst-stained nuclei in blue. Dashed lines indicate the regions used for fluorescence intensity profiling. Scale bar, 5 μm. **C**) Normalized Flag and Hoechst fluorescence intensity profiles along the dashed lines indicated in B. **D**) Nuclear-to-cytoplasmic Flag fluorescence intensity ratios for the indicated NUPR1 constructs. Each point represents one cell; data are presented as mean ± s.d. P values are indicated in the figure. Statistical significance was determined by

Langtaosha (LTS) Preprint doi: https://doi.org/10.65215/LTSpreprints.2026.11.14.000388. This version posted November 14, 2026. The copyright holder for this preprint (which was not certified by peer review) is the author/funder. Creative Commons license: CC Attribution-NonCommercial-NoDerivatives 4.0 https://creativecommons.org/licenses/by-nc-nd/4.0

one-way ANOVA followed by Tukey's multiple-comparisons test. **E**) Schematic workflow of FPPL. The POI is fused to a 12-amino-acid AAP, whereas ApbE is expressed separately and covalently transfers FMN from FAD to AAP. Upon blue-light irradiation (~450 nm), the protein-tethered flavin initiates local photochemical labeling of proximal proteins in the presence of an alkyne-containing probe. Labeled proteins are subsequently conjugated to azide-biotin by click chemistry, enriched, digested and identified by LC-MS/MS. Imaging experiments were repeated at least twice with consistent results.

A peptide-installed flavin enables photocatalytic proximity labeling in cells. Having established AAP as a minimally perturbative targeting element, we next asked whether it could be converted into a functional photocatalytic center. FPPL requires two sequential processes: ApbE-mediated covalent installation of FMN onto AAP, followed by light-dependent activation of the tethered flavin to drive local chemical labeling (Fig. 2A). Using purified MBP-AAP as a model substrate, increasing the ApbE molar ratio progressively increased in-gel FMN fluorescence, approaching maximal incorporation at an enzyme ratio of ~0.5 (Fig. 2B, D). At a 1:1 ratio, substantial FMN incorporation was detected within 2.5 min and approached a plateau around 20 min (Fig. 2C, E). ApbE efficiently modified AAP fused to either SUMO or MBP, whereas mutation of the acceptor threonine to alanine (AAP-T9A) markedly reduced FMN fluorescence in both contexts (Fig. 2F), establishing AAP as a compact and transferable substrate for sequence-dependent flavinylation.

We next sought to identify a chemical probe suitable for flavin-mediated proximity labeling. In a defined in vitro proximity assay, flavinylated SUMO–AAP–His was positioned adjacent to an anti-His antibody, allowing probe-dependent labeling of a neighboring protein to be evaluated (Supplementary Fig. 2A–D). This screen identified 3-ethynylaniline (3EA) as an

Langtaosha (LTS) Preprint doi: https://doi.org/10.65215/LTSpreprints.2026.11.14.000388. This version posted November 14, 2026. The copyright holder for this preprint (which was not certified by peer review) is the author/funder. Creative Commons license: CC Attribution-NonCommercial-NoDerivatives 4.0 https://creativecommons.org/licenses/by-nc-nd/4.0

effective alkyne-containing probe. We then evaluated a series of 3EA-related aromatic alkyne derivatives in cells using H2B–AAP as a nuclear model substrate. Among the compounds tested, 3E-4FA produced the strongest proteome-wide labeling signal following click conjugation to a rhodamine reporter (Fig. 2G; Supplementary Fig. 3A) and was therefore selected for subsequent FPPL experiments.

Using H2B–AAP, we next defined the requirements for cellular FPPL. H2B–AAP showed readily detectable flavin fluorescence, whereas untagged H2B did not, confirming AAP-dependent FMN installation in cells (Fig. 2H). In the presence of 3E-4FA, blue-light illumination produced robust rhodamine-detectable protein labeling, whereas omission of either the probe or light markedly reduced the signal. Labeling varied with probe concentration, and 450-nm illumination produced the strongest signal among the wavelengths tested (Supplementary Fig. 3B, C). Several AAP sequence variants substantially reduced or abolished FMN fluorescence (Supplementary Fig. 3D, E), further supporting the sequence dependence of cellular flavinylation.

We also examined whether increasing AAP copy number could improve labeling. H2B constructs bearing one or two AAP copies showed comparable FMN incorporation and proximity-labeling activity, whereas both signals were reduced with three or four repeats (Fig. 2I). AlphaFold 3 modeling of V5–ApbE–3×NLS with H2B bearing one to four AAPs yielded ipTM scores of 0.71, 0.69, 0.58 and 0.54, respectively, and the corresponding PAE maps provided no evidence that additional repeats generated progressively more favorable ApbE–substrate arrangements (Supplementary Fig. 4). Although these structural predictions do not directly measure flavin-transfer efficiency, they are consistent with the observation that increasing AAP copy number does not necessarily enhance productive ApbE engagement.

Langtaosha (LTS) Preprint doi: https://doi.org/10.65215/LTSpreprints.2026.11.14.000388. This version posted November 14, 2026. The copyright holder for this preprint (which was not certified by peer review) is the author/funder. Creative Commons license: CC Attribution-NonCommercial-NoDerivatives 4.0 https://creativecommons.org/licenses/by-nc-nd/4.0

Finally, we examined the photochemical basis of FPPL. Sodium azide and antioxidant reagents abolished labeling, whereas D_2O, which prolongs the lifetime of singlet oxygen in aqueous solution[51], enhanced the signal; vitamin C and mannitol also partially attenuated labeling (Supplementary Fig. 5). Together with the strict requirement for blue-light illumination, these results support the involvement of photoinduced reactive oxygen species and are consistent with a substantial contribution from singlet oxygen. Collectively, these findings establish that ApbE-mediated flavinylation converts AAP into a covalently tethered, light-responsive photocatalytic center capable of driving proximity-dependent protein labeling in living cells.

Langtaosha (LTS) Preprint doi: https://doi.org/10.65215/LTSpreprints.2026.11.14.000388. This version posted November 14, 2026. The copyright holder for this preprint (which was not certified by peer review) is the author/funder. Creative Commons license: CC Attribution-NonCommercial-NoDerivatives 4.0 https://creativecommons.org/licenses/by-nc-nd/4.0

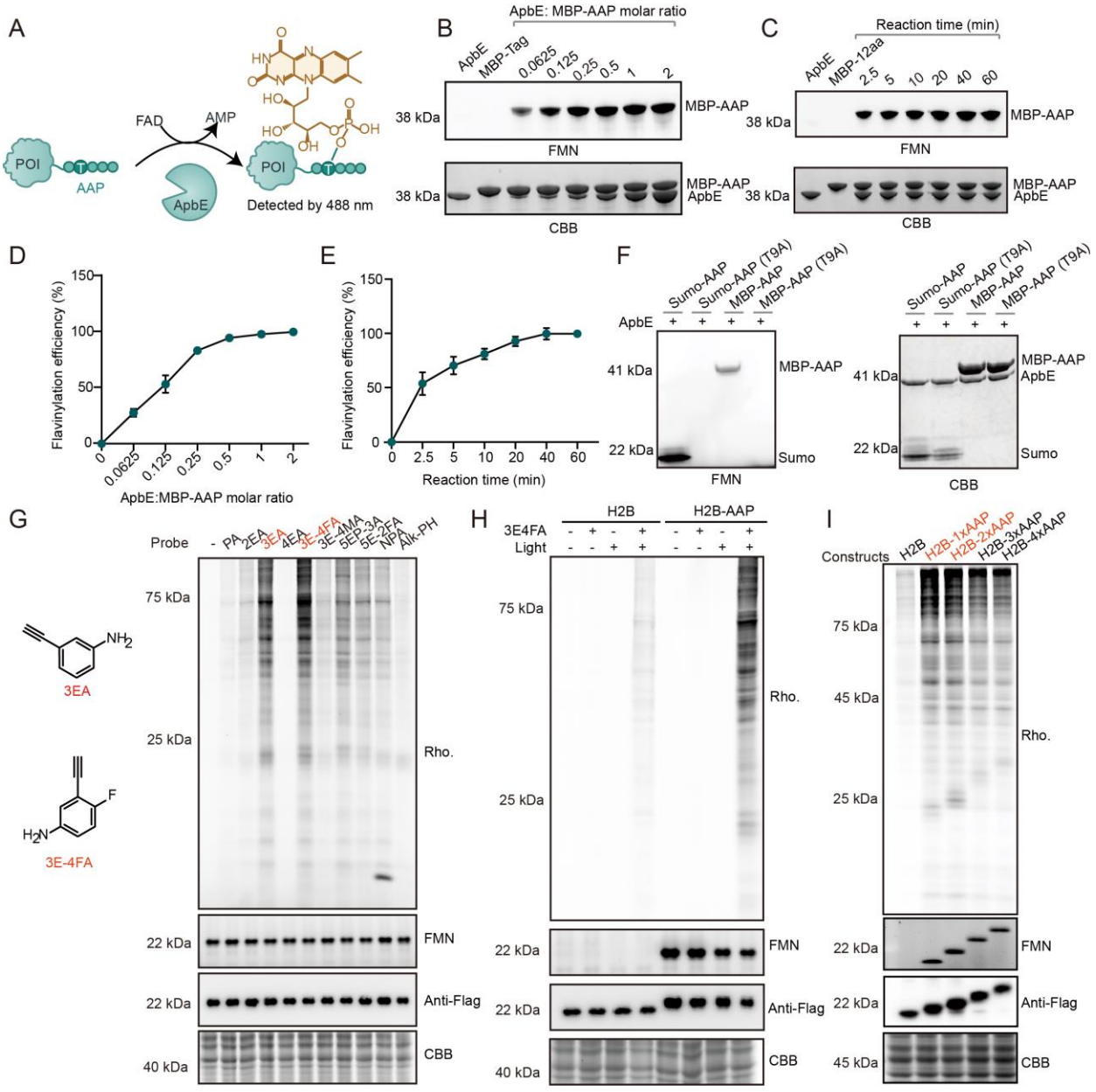


Fig. 2 Biochemical characterization and cellular validation of FPPL. A) Schematic of ApbE-mediated covalent FMN installation onto the 12-amino-acid AAP. **B**) *In vitro* flavinylation of MBP-AAP at the indicated ApbE-AAP molar ratios. FMN incorporation was detected by in-gel flavin fluorescence; CBB staining shows protein loading. **C**) Time course of ApbE-mediated FMN incorporation into MBP–AAP. **D, E**) Quantification of FMN fluorescence in B and C, respectively. Data are presented as mean ± s.d. from three biologically independent experiments. **F**) ApbE-mediated flavinylation of AAP fused to SUMO or MBP and the corresponding AAP(T9A) mutants. **G**) Cellular screening of aromatic alkyne probes using

Langtaosha (LTS) Preprint doi: https://doi.org/10.65215/LTSpreprints.2026.11.14.000388. This version posted November 14, 2026. The copyright holder for this preprint (which was not certified by peer review) is the author/funder. Creative Commons license: CC Attribution-NonCommercial-NoDerivatives 4.0 https://creativecommons.org/licenses/by-nc-nd/4.0

H2B–AAP. Probe labeling was detected by rhodamine fluorescence after click conjugation; flavin fluorescence, anti-Flag immunoblotting and CBB staining are shown as controls. Structures of 3EA and 3E-4FA are shown, with the remaining probe structures provided in Supplementary Fig. 2C. **H**) Dependence of cellular FPPL labeling on AAP, 3E-4FA and blue-light illumination in cells expressing H2B or H2B–AAP with nucleus-targeted ApbE. **I**) Effect of AAP copy number on FPPL using H2B constructs bearing one to four tandem AAPs. Proteome labeling, FMN incorporation and construct expression were monitored by rhodamine fluorescence, flavin fluorescence and anti-Flag immunoblotting, respectively. Experiments were repeated at least twice with consistent results.

Compartment-targeted FPPL enables spatially resolved proteome mapping. Having established cellular FPPL labeling, we next asked whether the system could preserve spatial information across distinct intracellular compartments. ApbE and AAP-bearing reporters were targeted to mitochondria, the cytosol-facing endoplasmic reticulum membrane (ERM), nucleoli and the nucleus (Fig. 3A). Compartment-targeted AAP reporters supported robust labeling and detectable FMN incorporation in mitochondrial, ERM and nuclear configurations (Supplementary Fig. 6). Fluorescence microscopy further revealed labeling patterns that matched the intended subcellular locations, including mitochondrial and ER-associated reticular structures, discrete nucleolar puncta and broader nuclear labeling (Fig. 3B). Fluorescence intensity profiling showed spatial correspondence between the Cy3 labeling signal, the Flag-tagged reporters and the corresponding compartment markers (Fig. 3C), indicating that FPPL can generate spatially restricted labeling in multiple intracellular environments.

We next used mitochondria as a benchmark to assess whether compartment-directed FPPL retained spatial selectivity at the proteome level. Cells expressing mitochondria-targeted ApbE

Langtaosha (LTS) Preprint doi: https://doi.org/10.65215/LTSpreprints.2026.11.14.000388. This version posted November 14, 2026. The copyright holder for this preprint (which was not certified by peer review) is the author/funder. Creative Commons license: CC Attribution-NonCommercial-NoDerivatives 4.0 https://creativecommons.org/licenses/by-nc-nd/4.0

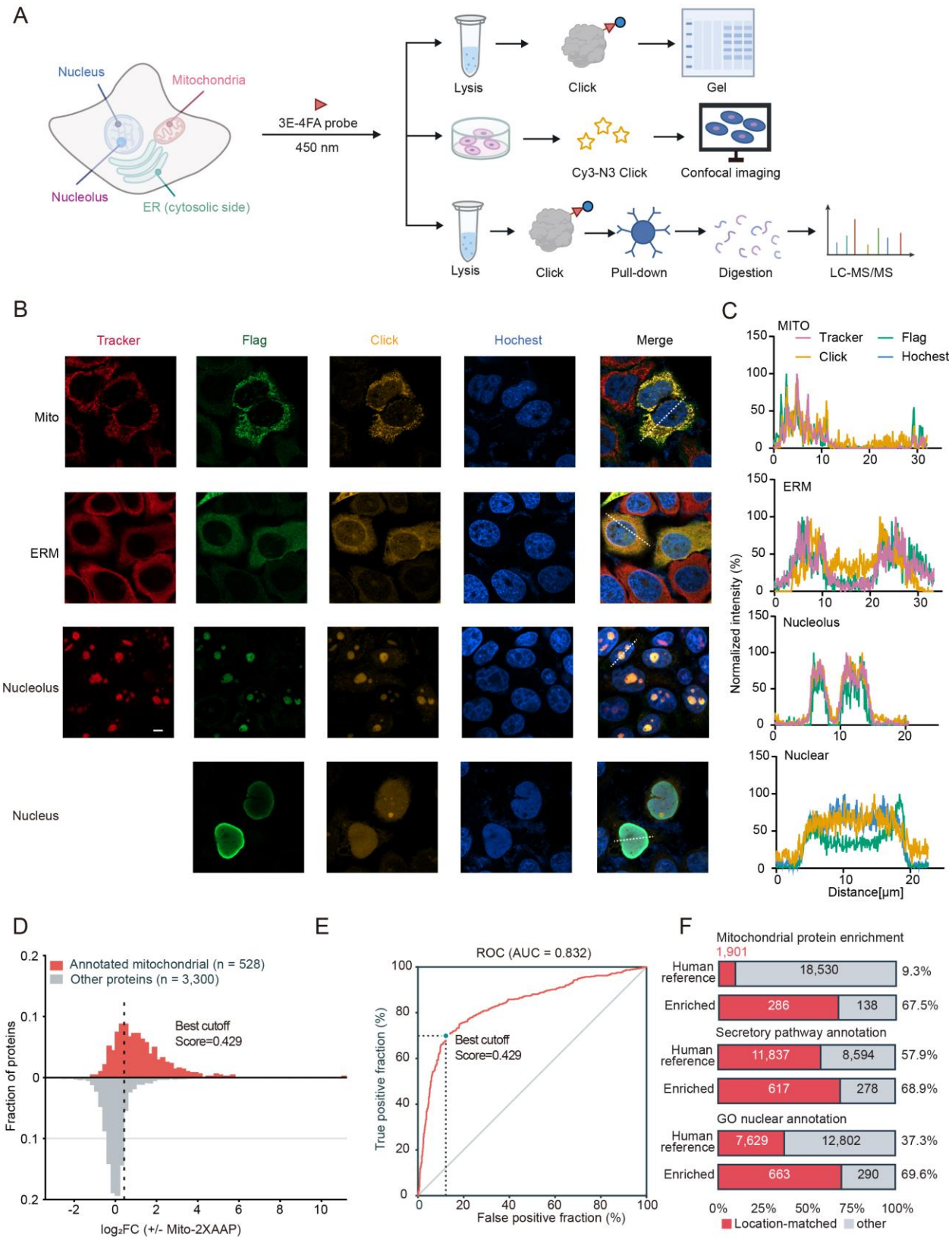
together with the corresponding AAP reporter were compared with matched controls, and labeled proteins were quantified by label-free LC–MS/MS. Mitochondrial reference proteins[52] were preferentially enriched relative to non-mitochondrial proteins[25], with ROC analysis yielding an AUC of 0.832 (Fig. 3D, E). Applying the ROC-derived enrichment threshold together with $P < 0.05$ identified 424 enriched proteins, of which 286 were annotated as mitochondrial. Mitochondrial proteins therefore constituted 67.5% of the enriched set, compared with 9.3% of the human reference proteome (Fig. 3F). These results indicate that mitochondria-directed FPPL preferentially enriches proteins associated with the targeted organelle environment. We next examined whether this spatial preference was retained at the submitochondrial level. Among the 286 enriched mitochondrial proteins, 201 were assigned to the matrix and 48 to the inner mitochondrial membrane, together accounting for 87.1% of the mitochondrial-enriched set (Supplementary Fig. 7F). By contrast, proteins assigned to the intermembrane space or outer mitochondrial membrane were much less represented. These results indicate that mitochondria-directed FPPL preferentially samples proteins within or near the matrix-facing mitochondrial environment.

We then extended quantitative proteomic profiling to the ER membrane and nucleus. ROC analysis yielded AUC values of 0.729 and 0.605 for ERM- and nucleus-directed FPPL, respectively (Supplementary Fig. 7D, E). Applying the ROC-derived threshold together with $P < 0.05$ identified 895 ERM-enriched proteins, of which 617 (68.9%) were assigned to the secretory pathway (Fig. 3F). We next characterized the sub-secretory specificity of the ERM-enriched proteome. Among detected proteins with Gene Ontology annotations for the ER, Golgi apparatus or plasma membrane, 41.6% (621 of 1,494) were assigned to the ER. By the same analysis, this proportion increased to 57.5% (227 of 395) in the ERM-enriched proteome (Supplementary Fig.

Langtaosha (LTS) Preprint doi: https://doi.org/10.65215/LTSpreprints.2026.11.14.000388. This version posted November 14, 2026. The copyright holder for this preprint (which was not certified by peer review) is the author/funder. Creative Commons license: CC Attribution-NonCommercial-NoDerivatives 4.0 https://creativecommons.org/licenses/by-nc-nd/4.0

243 7F), indicating preferential enrichment of ER-associated proteins over Golgi- and plasma
244 membrane-associated proteins. Similarly, 663 of the 953 nucleus-enriched proteins (69.6%)
245 carried nuclear annotations, compared with 37.3% in the human reference proteome (Fig. 3F).
246 Together, these data demonstrate that FPPL reproducibly enriches proteins associated with the
247 targeted intracellular environment across multiple subcellular compartments.

Langtaosha (LTS) Preprint doi: https://doi.org/10.65215/LTSpreprints.2026.11.14.000388. This version posted November 14, 2026. The copyright holder for this preprint (which was not certified by peer review) is the author/funder. Creative Commons license: CC Attribution-NonCommercial-NoDerivatives 4.0 https://creativecommons.org/licenses/by-nc-nd/4.0



248

Langtaosha (LTS) Preprint doi: https://doi.org/10.65215/LTSpreprints.2026.11.14.000388. This version posted November 14, 2026. The copyright holder for this preprint (which was not certified by peer review) is the author/funder. Creative Commons license: CC Attribution-NonCommercial-NoDerivatives 4.0 https://creativecommons.org/licenses/by-nc-nd/4.0

Fig. 3 Compartment-targeted FPPL enables spatially resolved labeling and proteome enrichment. A) Schematic of FPPL targeted to mitochondria, the cytosolic face of the ER membrane (ERM), nucleoli or the nucleus. Following 3E-4FA treatment and 450 nm illumination, labeled proteins were detected by streptavidin blotting, visualized by fluorescence imaging or enriched for LC–MS/MS analysis. **B**) Representative confocal images of cells expressing the corresponding compartment-targeted ApbE and AAP reporters. Cy3 labeling is shown in yellow, Flag in green, compartment markers or trackers in red and Hoechst in blue. Dashed lines indicate the paths used for fluorescence intensity profiling. Scale bar, 5 μm. **C**) Normalized fluorescence intensity profiles along the dashed lines in B. **D**) Distribution of $\log_2$ fold changes for MitoCarta-annotated mitochondrial proteins (n = 528) and other detected proteins (n = 3,300) in the mitochondrial FPPL dataset. The dashed line indicates the ROC-derived cutoff ($\log_2$ FC = 0.429). **E**) ROC analysis of mitochondrial protein enrichment (AUC = 0.832); the optimal cutoff was determined using the Youden index. **F**) Fraction of compartment-annotated proteins in the human reference proteome and the corresponding FPPL-enriched sets. Mitochondrial proteins represented 67.5% of the enriched mitochondrial set versus 9.3% of the reference proteome; secretory-pathway proteins represented 68.9% of the ERM-enriched set versus 57.9% of the reference proteome; and nuclear proteins represented 69.6% of the nucleus-enriched set versus 37.3% of the reference proteome. Enriched proteins were defined using the corresponding ROC-derived $\log_2$ FC cutoffs together with $P < 0.05$. Proteomic measurements were obtained from three biological replicates. Imaging and biochemical experiments were repeated at least twice with consistent results.

FPPL defines the proximal protein network of BANF1. We next applied FPPL to BANF1, an 89-amino-acid DNA-binding protein with established roles in chromatin organization, postmitotic nuclear-envelope assembly and nuclear-envelope rupture repair[48,53-56]. Because these functions depend extensively on its local protein environment, BANF1 provided a suitable model for testing

Langtaosha (LTS) Preprint doi: https://doi.org/10.65215/LTSpreprints.2026.11.14.000388. This version posted November 14, 2026. The copyright holder for this preprint (which was not certified by peer review) is the author/funder. Creative Commons license: CC Attribution-NonCommercial-NoDerivatives 4.0 https://creativecommons.org/licenses/by-nc-nd/4.0

whether peptide-scale proximity labeling could resolve a biologically informative protein network around a compact protein.

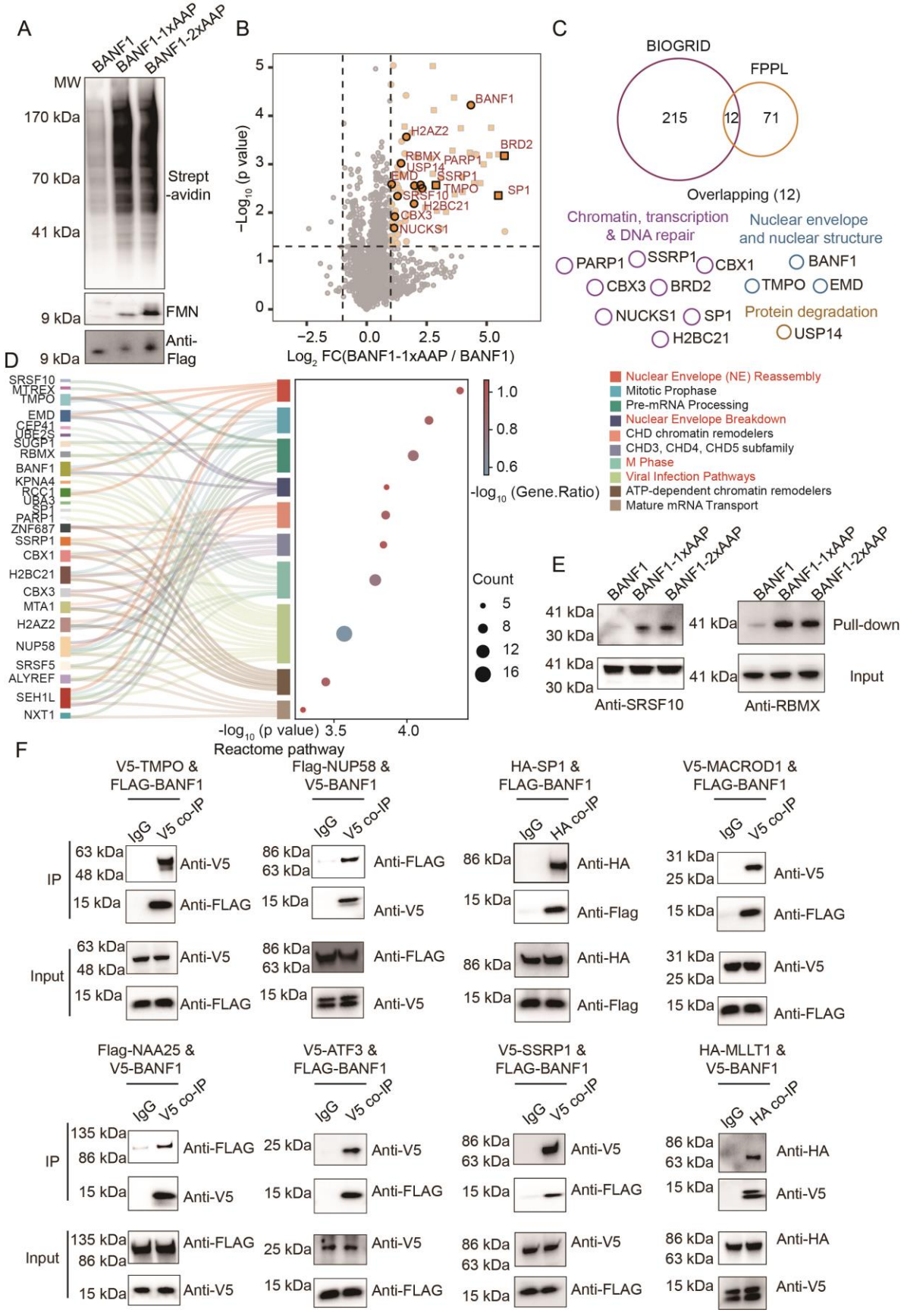
Both BANF1-AAP and BANF1-2×AAP supported FMN incorporation and biotin-detectable protein labeling above the untagged BANF1 background (Fig. 4A). We therefore selected BANF1-AAP for quantitative proteomic analysis to retain the minimal peptide fusion and compared it with untagged BANF1 processed under the same labeling and enrichment conditions. Label-free LC–MS/MS identified proteins enriched by more than twofold with $P < 0.05$ (Fig. 4B), defining a set of FPPL-enriched BANF1-proximal candidates for subsequent network analysis and validation. Comparison with curated BANF1 interaction records in BioGRID[57] showed that 12 proteins were shared between the two datasets, whereas 71 FPPL-enriched proteins were not represented in the BioGRID dataset used for comparison (Fig. 4C). Functional analysis of the FPPL-enriched proteins highlighted nuclear-envelope reassembly and breakdown, mitotic regulation, chromatin remodeling and pre-mRNA processing (Fig. 4D). These functional categories are consistent with established roles of BANF1 in coordinating chromatin and nuclear-envelope organization, while also extending the proximity-defined network to additional nuclear factors. Because proximity labeling reports the local molecular environment rather than physical interactions, these proteins were considered candidate BANF1-proximal factors for further evaluation.

We next examined representative candidates using complementary biochemical assays. Streptavidin enrichment followed by immunoblotting confirmed preferential FPPL labeling of SRSF10 and RBMX, two nuclear RNA-processing proteins, supporting their proximity to BANF1 (Fig. 4E). Co-immunoprecipitation further confirmed associations between BANF1 and TMPO/LAP2, NUP58, SP1, MACROD1, NAA25, ATF3, SSRP1 and MLLT1/ENL, which

Langtaosha (LTS) Preprint doi: https://doi.org/10.65215/LTSpreprints.2026.11.14.000388. This version posted November 14, 2026. The copyright holder for this preprint (which was not certified by peer review) is the author/funder. Creative Commons license: CC Attribution-NonCommercial-NoDerivatives 4.0 https://creativecommons.org/licenses/by-nc-nd/4.0

296 participate in nuclear-envelope organization, nuclear transport, transcriptional regulation,
297 chromatin remodeling and protein modification (Fig. 4F). Together, these analyses define a
298 BANF1-centered protein network supported by proximity labeling and complementary association
299 assays and provide a focused set of candidates for subsequent functional interrogation.

Langtaosha (LTS) Preprint doi: https://doi.org/10.65215/LTSpreprints.2026.11.14.000388. This version posted November 14, 2026. The copyright holder for this preprint (which was not certified by peer review) is the author/funder. Creative Commons license: CC Attribution-NonCommercial-NoDerivatives 4.0 https://creativecommons.org/licenses/by-nc-nd/4.0



300

Langtaosha (LTS) Preprint doi: https://doi.org/10.65215/LTSpreprints.2026.11.14.000388. This version posted November 14, 2026. The copyright holder for this preprint (which was not certified by peer review) is the author/funder. Creative Commons license: CC Attribution-NonCommercial-NoDerivatives 4.0 https://creativecommons.org/licenses/by-nc-nd/4.0

Fig. 4 FPPL maps the proximal protein network of BANF1. A) Streptavidin blot of cells expressing BANF1, BANF1–AAP or BANF1–2×AAP. FMN fluorescence and anti-Flag immunoblotting show AAP flavinylation and construct expression, respectively. **B**) Volcano plot of label-free proteomic enrichment for BANF1–AAP relative to untagged BANF1. Dashed lines indicate twofold enrichment and P = 0.05; representative enriched proteins are labeled. Data are from three biological replicates. **C**) Comparison of FPPL-enriched proteins with BANF1-associated proteins in BioGRID. Twelve proteins were shared between the datasets, with 71 unique to the FPPL dataset and 215 unique to BioGRID. Representative shared proteins are grouped by the indicated functional categories. **D**) Reactome analysis of the BANF1-proximal proteome. The alluvial plot links selected enriched proteins to representative pathways; bubble size indicates protein count and color corresponds to the enrichment metric shown. **E**) NeutrAvidin enrichment followed by immunoblotting for SRSF10 and RBMX in the indicated BANF1 samples. Inputs are shown below. **F**) Co-immunoprecipitation analysis of selected FPPL-identified BANF1-associated proteins. IgG immunoprecipitation served as a negative control; corresponding input lysates are shown. Experiments were repeated at least twice with consistent results.

Functional convergence of the BANF1 proximal network on nuclear-envelope integrity. The enrichment of nuclear-envelope and chromatin-associated pathways within the BANF1 proximal proteome suggested that the network captured by FPPL might contain functionally relevant determinants of nuclear-envelope homeostasis. We therefore asked whether perturbing FPPL-identified BANF1-interacting proteins would reveal a shared requirement for maintaining nuclear compartmentalization. To address this, we used RPE-1 reporter cells expressing GFP–BANF1, with or without a nuclear RFP–NLS reporter[58] (Fig. 5A; Supplementary Figs. 9A and 10A). In cells with an intact nuclear envelope, RFP–NLS remained confined to the nucleus and GFP–BANF1 was predominantly diffuse. Nuclear-envelope disruption was accompanied by

Langtaosha (LTS) Preprint doi: https://doi.org/10.65215/LTSpreprints.2026.11.14.000388. This version posted November 14, 2026. The copyright holder for this preprint (which was not certified by peer review) is the author/funder. Creative Commons license: CC Attribution-NonCommercial-NoDerivatives 4.0 https://creativecommons.org/licenses/by-nc-nd/4.0

cytoplasmic leakage of RFP–NLS and focal accumulation of GFP–BANF1, providing complementary readouts of loss of nuclear compartmentalization and recruitment of BANF1 to sites of envelope damage.

We selected eight FPPL-identified candidates that were supported by co-immunoprecipitation—MLLT1, SP1, SSRP1, ATF3, NUP58, NAA25, TMPO and MACROD1—and depleted each using two independent siRNAs. RT–qPCR confirmed reduced expression of the targeted transcripts (Supplementary Fig. 8). Depletion of MLLT1, SP1, SSRP1, ATF3, NUP58, NAA25 or TMPO consistently increased the fraction of cells containing GFP–BANF1 foci relative to siControl (Fig. 5B; Supplementary Fig. 9A–C). Importantly, the same perturbations also increased the proportion of cells displaying both focal GFP–BANF1 accumulation and cytoplasmic RFP–NLS leakage (Fig. 5C; Supplementary Fig. 10A, B), linking BANF1 recruitment to a measurable breakdown of nuclear compartmentalization. MACROD1 depletion produced a substantially weaker phenotype under the same conditions. Thus, seven of the eight tested FPPL candidates converged on a common nuclear-envelope integrity phenotype despite representing functionally diverse nuclear processes.

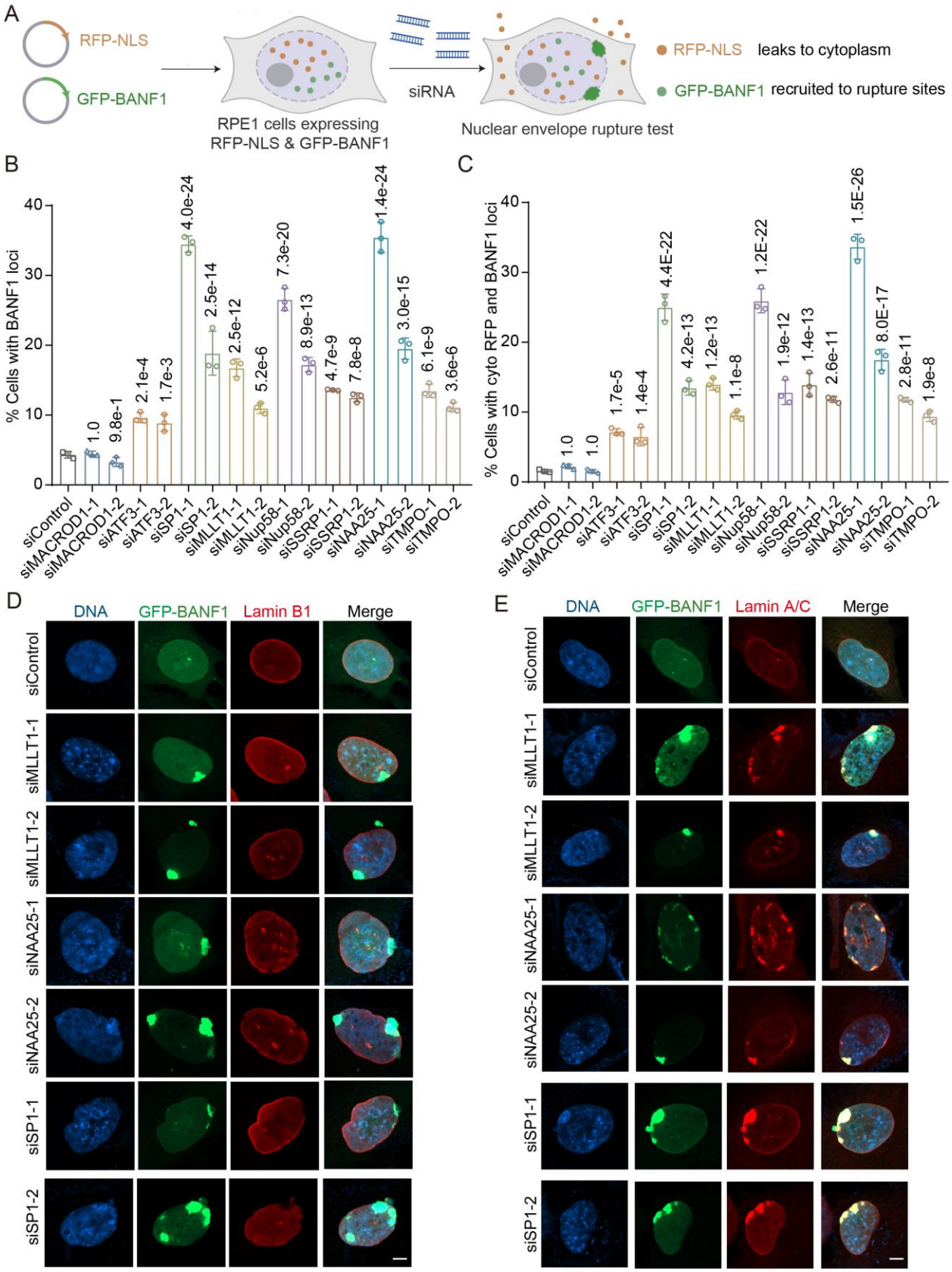
We next examined whether this loss of compartmentalization was accompanied by structural remodeling of the nuclear lamina. In cells depleted of MLLT1, NAA25 and SP1, GFP–BANF1 foci localized to regions showing altered or discontinuous Lamin B1 staining (Fig. 5D; Supplementary Fig. 11). Lamin A/C similarly displayed focal redistribution at GFP–BANF1-positive regions (Fig. 5E). Comparable patterns were observed following depletion of SSRP1, NUP58, ATF3 and TMPO, whereas MACROD1-depleted cells more closely resembled the control in representative fields (Supplementary Fig. 11). These observations connect the reporter-based

Langtaosha (LTS) Preprint doi: https://doi.org/10.65215/LTSpreprints.2026.11.14.000388. This version posted November 14, 2026. The copyright holder for this preprint (which was not certified by peer review) is the author/funder. Creative Commons license: CC Attribution-NonCommercial-NoDerivatives 4.0 https://creativecommons.org/licenses/by-nc-nd/4.0

loss of nuclear compartmentalization with local reorganization of the lamina at sites of BANF1 accumulation.

Together, these results reveal functional convergence within the BANF1 proximal network, as depletion of diverse BANF1-associated factors led to nuclear reporter leakage, focal BANF1 recruitment and local lamina remodeling. These findings place BANF1 within a broader nuclear homeostatic network in which multiple molecular processes cooperate to maintain nuclear-envelope integrity.

Langtaosha (LTS) Preprint doi: https://doi.org/10.65215/LTSpreprints.2026.11.14.000388. This version posted November 14, 2026. The copyright holder for this preprint (which was not certified by peer review) is the author/funder. Creative Commons license: CC Attribution-NonCommercial-NoDerivatives 4.0 https://creativecommons.org/licenses/by-nc-nd/4.0



Langtaosha (LTS) Preprint doi: https://doi.org/10.65215/LTSpreprints.2026.11.14.000388. This version posted November 14, 2026. The copyright holder for this preprint (which was not certified by peer review) is the author/funder. Creative Commons license: CC Attribution-NonCommercial-NoDerivatives 4.0 https://creativecommons.org/licenses/by-nc-nd/4.0

Fig. 5 Functional interrogation of the BANF1- associated proteins identifies regulators of nuclear-envelope integrity. A) Schematic of the reporter assay in RPE-1 cells expressing GFP–BANF1 and RFP–NLS. Nuclear-envelope disruption is monitored by focal GFP–BANF1 accumulation and cytoplasmic redistribution of RFP–NLS following siRNA-mediated depletion of candidate proteins. **B**, **C**) Quantification of cells containing GFP–BANF1 foci (B) or both GFP–BANF1 foci and cytoplasmic RFP–NLS (C) after depletion of the indicated proteins. Data are mean ± s.d. from three biologically independent experiments, with >200 cells analyzed per condition. P values were determined by one-way ANOVA followed by Dunnett's multiple-comparisons test versus siControl. **D, E**) Representative fluorescence images showing GFP–BANF1 localization together with Lamin B1 (D) or Lamin A/C (E) following depletion of the indicated proteins. GFP–BANF1 foci coincide with local alterations in nuclear-lamina organization. DNA, GFP–BANF1 and lamins are shown in blue, green and red, respectively. Scale bars, 5 μm. Experiments were repeated three times with consistent results.

FPPL reveals an unexpected virus-associated protein network around GNG4. We next asked whether FPPL could uncover functional protein networks around a compact signaling protein outside the nuclear context. We selected GNG4, a 75-amino-acid γ subunit of heterotrimeric G proteins whose molecular environment remains incompletely defined[59]. GNG4 fused to intact AAP supported robust light-dependent proximity labeling, whereas the non-flavinylatable AAP(T9A) mutant showed markedly reduced labeling despite comparable protein expression (Fig. 6A). We therefore used AAP(T9A) as a sequence-matched reference for quantitative proteomics. Comparison of GNG4–AAP with GNG4–AAP(T9A) identified 83 FPPL-enriched proximal candidates at the defined statistical threshold (Fig. 6B).

Functional inspection of this dataset revealed an unexpected enrichment of proteins previously linked to virus–host interactions (Fig. 6C). Literature-based curation identified 27 of

Langtaosha (LTS) Preprint doi: https://doi.org/10.65215/LTSpreprints.2026.11.14.000388. This version posted November 14, 2026. The copyright holder for this preprint (which was not certified by peer review) is the author/funder. Creative Commons license: CC Attribution-NonCommercial-NoDerivatives 4.0 https://creativecommons.org/licenses/by-nc-nd/4.0

379 the 83 candidates (32.5%) with reported roles in viral infection or antiviral responses, including
380 12 classified as proviral, 8 as antiviral and 7 with context-dependent or bidirectional functions (Fig.
381 6D). Proviral candidates included VDAC1, which enhances infectious bursal disease virus
382 polymerase activity[60], and VTA1, an ESCRT-associated factor involved in HCV assembly and
383 HIV-1 budding[61,62]. Among antiviral regulators, PPP1R12C promotes RIG-I-like receptor
384 activation[63], while EXOC4 (Sec8) enhances antiviral signaling by stabilizing STING1 and RIG-I
385 [64,65] . IKBKG (NEMO), a key mediator of antiviral signaling, is targeted by SARS-CoV-2 ORF9b
386 to suppress innate immunity[66], whereas MTCH2 interacts with influenza A virus PA and restricts
387 viral replication[67]. Notably, ARF6 exhibits virus-dependent functions, facilitating SARS-CoV-2
388 pseudovirus entry through CD147-associated trafficking[68] while restricting coxsackievirus B3
389 infection by directing viral particles into nonproductive endosomal compartments[69]. Similarly,
390 FANCD2 supports HSV-1 DNA replication but can restrict HPV genome amplification,
391 highlighting its context-dependent roles in viral infection[70,71]. Together, these findings revealed an
392 unexpected host–virus-associated network around GNG4 spanning distinct cellular processes.

393 We next validated representative candidates by co-immunoprecipitation. GNG4
394 reproducibly associated with PPP1R12C, EXOC4, ARF6, IKBKG, MTCH2 and RABEP2 (an
395 endosomal trafficking regulator[72]) (Fig. 6E), providing independent support for their identification
396 in the FPPL-defined network. The convergence of several independently implicated antiviral
397 regulators within the GNG4 proximal proteome prompted us to investigate whether GNG4 itself
398 contributes to innate antiviral signaling.

399

Langtaosha (LTS) Preprint doi: https://doi.org/10.65215/LTSpreprints.2026.11.14.000388. This version posted November 14, 2026. The copyright holder for this preprint (which was not certified by peer review) is the author/funder. Creative Commons license: CC Attribution-NonCommercial-NoDerivatives 4.0 https://creativecommons.org/licenses/by-nc-nd/4.0

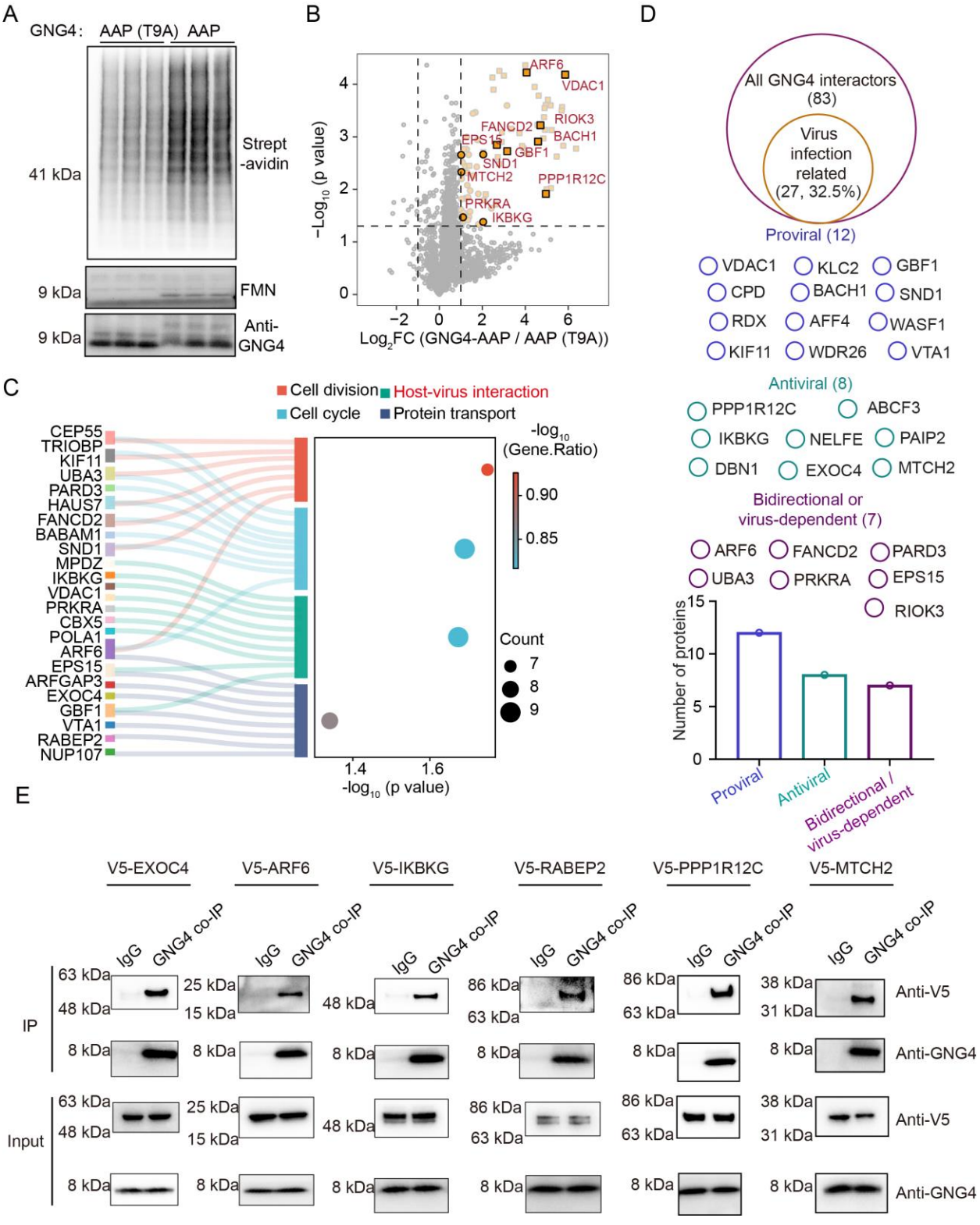


Fig. 6 FPPL reveals a virus-associated proximal network of GNG4. A) Evaluation of FPPL labeling using GNG4–AAP and the non-flavinylatable GNG4–AAP(T9A) control. Biotinylated proteins were

Langtaosha (LTS) Preprint doi: https://doi.org/10.65215/LTSpreprints.2026.11.14.000388. This version posted November 14, 2026. The copyright holder for this preprint (which was not certified by peer review) is the author/funder. Creative Commons license: CC Attribution-NonCommercial-NoDerivatives 4.0 https://creativecommons.org/licenses/by-nc-nd/4.0

403 detected by streptavidin blotting, whereas FMN fluorescence and anti-Flag immunoblotting were used to
404 monitor AAP flavinylation and construct expression, respectively. **B**) Volcano plot of quantitative
405 proteomic enrichment in GNG4–AAP relative to GNG4–AAP(T9A). Representative FPPL-enriched
406 proteins, including candidates selected for subsequent validation are labeled. **C**) Functional annotation of
407 the GNG4 proximal proteome. The alluvial plot links selected enriched proteins to representative functional
408 categories, including cell-cycle regulation, host–virus interactions and protein transport; the accompanying
409 bubble plot summarizes pathway enrichment. **D**) Classification of virus-associated proteins within the
410 GNG4 proximal proteome. Among 83 FPPL-enriched proteins, 27 (32.5%) had reported roles in virus-
411 related processes and were classified as proviral, antiviral or context-dependent factors. **E**) Co-
412 immunoprecipitation analysis of selected FPPL-identified GNG4-associated proteins. Cells co-expressing
413 GNG4 and the indicated candidate proteins were subjected to anti-GNG4 immunoprecipitation followed
414 by immunoblotting. IgG served as a negative control and corresponding input lysates are shown.
415 Experiments were repeated at least twice with similar results.

416

417 **A GNG4-centered proximal network promotes antiviral signaling.** The unexpected
418 representation of virus-associated proteins within the GNG4 proximal proteome prompted us to
419 test whether GNG4 itself participates in innate antiviral signaling. We stimulated cells with Sendai
420 virus (SeV), a commonly used activator of RIG-I–MAVS signaling[73]. GNG4 overexpression
421 enhanced SeV-induced STAT1 phosphorylation without appreciably altering total STAT1 levels
422 and further increased induction of *IFNB1* and the interferon-stimulated gene *IFIT1* (Fig. 7A–C).
423 Conversely, depletion of GNG4 with two independent siRNAs markedly reduced SeV-induced
424 STAT1 phosphorylation as well as *IFNB1* and *IFIT1* expression (Fig. 7D–F), with efficient
425 knockdown confirmed by RT–qPCR (Supplementary Fig. 12A). These complementary gain- and
426 loss-of-function experiments identify GNG4 as a previously unrecognized positive regulator of the

Langtaosha (LTS) Preprint doi: https://doi.org/10.65215/LTSpreprints.2026.11.14.000388. This version posted November 14, 2026. The copyright holder for this preprint (which was not certified by peer review) is the author/funder. Creative Commons license: CC Attribution-NonCommercial-NoDerivatives 4.0 https://creativecommons.org/licenses/by-nc-nd/4.0

antiviral response. Notably, the effect on *IFNB1* induction places the contribution of GNG4 at or upstream of interferon production rather than solely at the level of downstream STAT1 activation.

We next asked whether proteins identified within the GNG4 proximal network were functionally connected to this response. Overexpression of the FPPL-identified candidates MTCH2 or ARF6 enhanced SeV-induced STAT1 phosphorylation (Fig. 7G, H). More importantly, expression of either protein in GNG4-depleted cells partially restored *IFNB1* and *IFIT1* induction and rescued STAT1 phosphorylation following SeV stimulation (Fig. 7I–K). Thus, MTCH2 and ARF6 can partially bypass the signaling defect caused by GNG4 loss, supporting functional convergence between GNG4 and components of its proximal protein network.

This relationship extended beyond MTCH2 and ARF6. Immunoblot analysis showed stronger SeV-induced STAT1 phosphorylation upon overexpression of RABEP2, EXOC4 or PPP1R12C, whereas IKBKG did not appreciably increase the signal (Supplementary Fig. 12B–E). In GNG4-depleted cells, RABEP2, EXOC4 and PPP1R12C increased pSTAT1 signals to differing extents, while IKBKG showed little effect (Supplementary Fig. 12F–I). RT–qPCR analyses further showed that overexpression of ARF6, EXOC4, MTCH2, RABEP2 and PPP1R12C enhanced SeV-induced *IFNB1* and *IFIT1* expression, whereas IKBKG did not show comparable enhancement of both transcripts (Supplementary Fig. 13A–L). Together, these results support a GNG4-centered network in which several proximal candidates modulate virus-induced interferon responses, providing functional support for the antiviral signature revealed by FPPL. The convergence of several membrane- and trafficking-associated GNG4-proximal proteins further suggests that GNG4 may couple membrane organization or intracellular trafficking to efficient innate immune signaling, revealing an unexpected signaling function for a heterotrimeric G-protein γ subunit.

Langtaosha (LTS) Preprint doi: https://doi.org/10.65215/LTSpreprints.2026.11.14.000388. This version posted November 14, 2026. The copyright holder for this preprint (which was not certified by peer review) is the author/funder. Creative Commons license: CC Attribution-NonCommercial-NoDerivatives 4.0 https://creativecommons.org/licenses/by-nc-nd/4.0

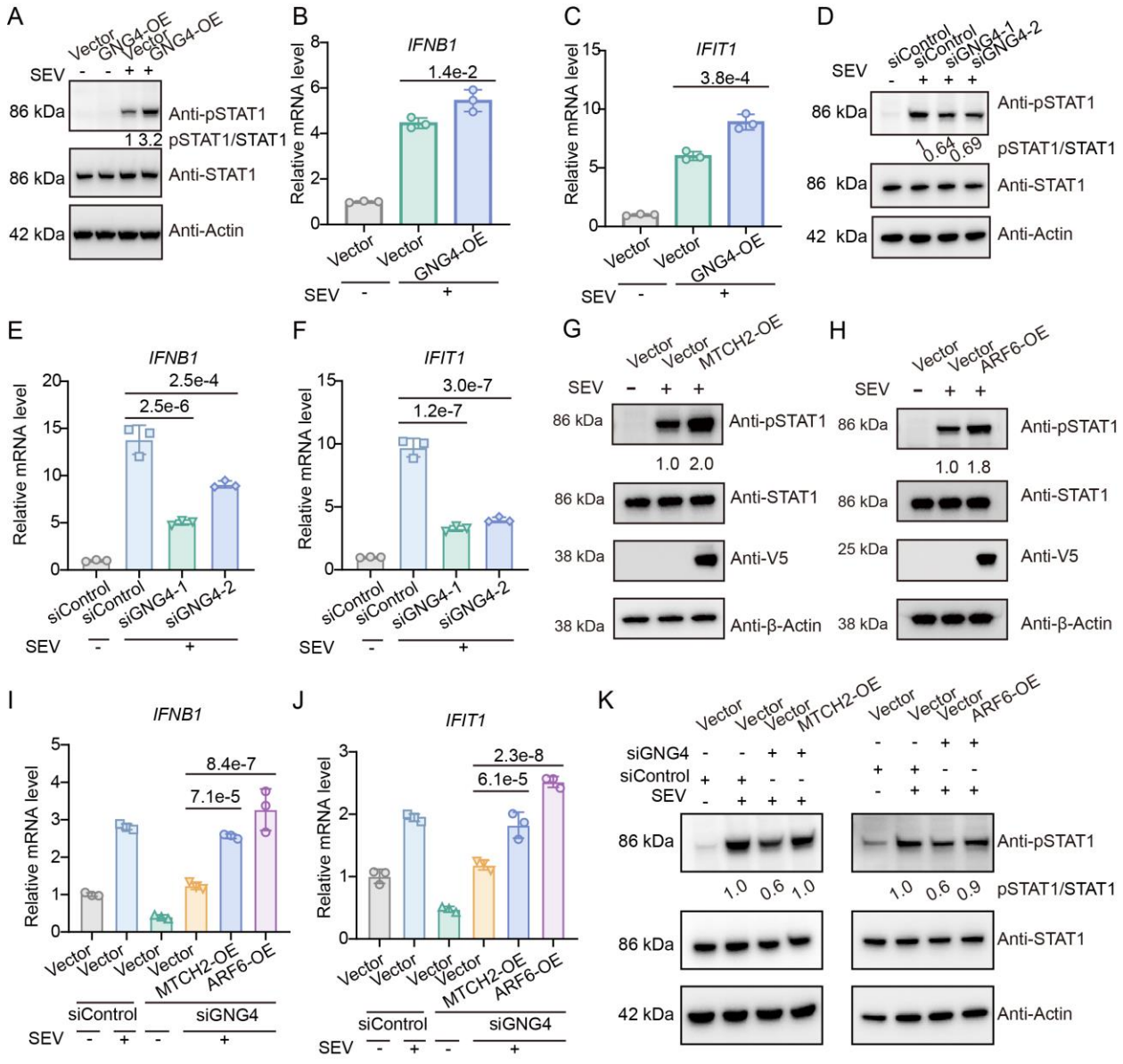


Fig. 7 GNG4 and its proximal protein network promote antiviral signaling. A) Immunoblot analysis of SeV-induced STAT1 phosphorylation in vector-control or GNG4-overexpressing cells. Total STAT1 and actin are shown as controls; relative pSTAT1/STAT1 ratios are indicated. **B, C)** RT–qPCR analysis of *IFNB1* (B) and *IFIT1* (C) expression following GNG4 overexpression and SeV stimulation. **D)** Immunoblot analysis of SeV-induced STAT1 phosphorylation following depletion of GNG4 with two independent siRNAs. Relative pSTAT1/STAT1 ratios are indicated. **E, F)** RT–qPCR analysis of *IFNB1* (E) and *IFIT1* (F) following GNG4 depletion and SeV stimulation. **G, H)** Effects of MTCH2 (G) or ARF6 (H)

Langtaosha (LTS) Preprint doi: https://doi.org/10.65215/LTSpreprints.2026.11.14.000388. This version posted November 14, 2026. The copyright holder for this preprint (which was not certified by peer review) is the author/funder. Creative Commons license: CC Attribution-NonCommercial-NoDerivatives 4.0 https://creativecommons.org/licenses/by-nc-nd/4.0

457 overexpression on SeV-induced STAT1 phosphorylation. Candidate expression was monitored by anti-V5
458 immunoblotting. **I, J)** RT–qPCR analysis of *IFNB1* (I) and *IFIT1* (J) following expression of MTCH2 or
459 ARF6 in GNG4-depleted cells after SeV stimulation. **K)** Immunoblot analysis of SeV-induced STAT1
460 phosphorylation in GNG4-depleted cells expressing MTCH2 or ARF6. Relative pSTAT1/STAT1 ratios are
461 indicated. RT–qPCR data are presented as mean ± s.d. from three biologically independent experiments,
462 with P values indicated above the bars. Immunoblotting experiments were repeated at least twice with
463 similar results.

464

465 **DISCUSSION**

466 Here we establish the FPPL platform, a proximity-proteomics strategy that decouples
467 photocatalyst installation from the protein of interest. Conventional genetically encoded
468 proximity-labeling systems generally require direct fusion of a protein-sized enzyme to the target,
469 which can impose a substantial structural burden on compact proteins. In FPPL, the target carries
470 only the 12-amino-acid AAP, whereas ApbE is supplied separately to covalently install FMN and
471 generate a protein-tethered photocatalytic center. AAP was rapidly and efficiently flavinylated by
472 ApbE, displaying favorable modification kinetics in vitro and robust FMN incorporation in cells,
473 supporting its use as a compact and readily installed photocatalytic module. Consistent with this
474 design, AAP fusion preserved the localization of NUPR1 and BANF1 substantially better than
475 direct TurboID fusion, while compartment-targeted FPPL retained spatial information at both
476 imaging and proteomic levels. Thus, the key feature of FPPL is not simply a smaller targeting
477 element, but the physical separation of the cofactor-installation machinery from the target while
478 retaining a covalently anchored photocatalyst at the protein of interest.

Langtaosha (LTS) Preprint doi: https://doi.org/10.65215/LTSpreprints.2026.11.14.000388. This version posted November 14, 2026. The copyright holder for this preprint (which was not certified by peer review) is the author/funder. Creative Commons license: CC Attribution-NonCommercial-NoDerivatives 4.0 https://creativecommons.org/licenses/by-nc-nd/4.0

This architecture is chemically distinct from other strategies developed to reduce the genetic footprint of proximity labeling. ASAP-ID uses short peptide epitopes to recruit antibody-linked labeling enzymes[42], whereas FPPL installs the photocatalytic cofactor directly onto the target-associated peptide and therefore does not require persistent recruitment of a protein-sized labeling enzyme. FlAsH-ID provides an even closer conceptual comparison because it also converts a short peptide into a photocatalytic labeling site[74,75]. However, FlAsH-ID relies on binding of an exogenously supplied biarsenical fluorophore to a tetracysteine motif, whereas FPPL uses ApbE-catalyzed covalent transfer of FMN to a defined acceptor peptide. Biarsenical–tetracysteine systems have long required thiol-blocking or dithiol-washing procedures to suppress nonspecific cellular binding[76-80]; FPPL instead relies on enzyme-defined covalent flavin installation and does not depend on equilibrium association of the photocatalyst with the target peptide. Moreover, biarsenical labeling depends on reduced cysteine thiols and can be challenging in oxidizing cellular environments, as demonstrated by the requirement for reducing agents to label tetracysteine-tagged proteins within the Golgi lumen[81]. In contrast, FPPL avoids the requirement for a reduced tetracysteine motif and may alleviate redox-dependent constraints on photocatalyst installation. We do not infer from this distinction that FPPL necessarily has lower background without direct comparison, but the two systems provide fundamentally different solutions to peptide-scale photocatalyst installation. Together with previous work showing that ApbE can be repurposed for engineered covalent flavin incorporation[32,33], our results establish enzymatic flavinylation as a programmable route for constructing genetically specified photocatalytic centers in living cells.

Application of FPPL to BANF1 illustrates how a proximity-defined protein environment can be connected to cellular function. The BANF1 proximal proteome contained proteins linked

Langtaosha (LTS) Preprint doi: https://doi.org/10.65215/LTSpreprints.2026.11.14.000388. This version posted November 14, 2026. The copyright holder for this preprint (which was not certified by peer review) is the author/funder. Creative Commons license: CC Attribution-NonCommercial-NoDerivatives 4.0 https://creativecommons.org/licenses/by-nc-nd/4.0

to chromatin organization, nuclear-envelope remodeling and RNA processing, and several candidates were supported by complementary biochemical assays. Functional interrogation further showed that depletion of seven of eight tested candidates increased nuclear reporter leakage, focal BANF1 accumulation and local lamina remodeling. The convergence of functionally diverse proteins on a common nuclear-envelope phenotype suggests that BANF1 operates within a broader nuclear homeostatic network in which chromatin regulation, nuclear transport and envelope organization collectively preserve nuclear compartmentalization. This network-level view extends the established role of BANF1 in nuclear-envelope repair and illustrates how proximity proteomics can reveal functional organization around compact proteins.

The GNG4 study highlights a complementary strength of FPPL: the ability to uncover biological functions that are not readily predicted from the canonical annotation of the target protein. Nearly one-third of the GNG4 proximal proteome consisted of proteins previously linked to virus–host processes, leading us to identify GNG4 as a positive regulator of SeV-induced *IFNB1* expression, *IFIT1* induction and STAT1 phosphorylation. The effect on *IFNB1* indicates that GNG4 influences the antiviral response at or upstream of interferon production rather than acting solely through downstream STAT1 signaling. Multiple GNG4-proximal proteins, including MTCH2, ARF6, EXOC4 and RABEP2, similarly enhanced antiviral responses, while MTCH2 and ARF6 partially restored signaling in GNG4-depleted cells. These findings support a functionally connected GNG4-centered antiviral network and raise the possibility that GNG4 links membrane-associated or trafficking processes to innate immune signaling.

Together, these studies establish FPPL as a peptide-scale strategy for mapping and functionally interrogating the molecular environments of compact proteins. The combination of minimal genetic modification, covalent photocatalyst installation and spatially restricted

Langtaosha (LTS) Preprint doi: https://doi.org/10.65215/LTSpreprints.2026.11.14.000388. This version posted November 14, 2026. The copyright holder for this preprint (which was not certified by peer review) is the author/funder. Creative Commons license: CC Attribution-NonCommercial-NoDerivatives 4.0 https://creativecommons.org/licenses/by-nc-nd/4.0

proteomic labeling should facilitate applications to endogenous proteins and other systems in which conventional enzyme fusions are difficult to accommodate. Further development of engineered ApbE–AAP pairs, alternative flavin photocatalysts and improved trapping chemistries may extend the efficiency, spatial resolution and cellular scope of the platform. More broadly, FPPL provides a route from minimally perturbative proximity mapping to functional hypothesis generation for proteins whose biology is encoded by their local molecular context.

Methods

Cell culture. HEK293T (ATCC CRL-3216), HeLa (ATCC CRM-CCL-2) and hTERT RPE-1 (ATCC CRL-4000) cells were maintained at 37 °C in a humidified incubator with 5% CO_2. HEK293T and HeLa cells were cultured in DMEM supplemented with 10% fetal bovine serum (FBS) and 1% penicillin–streptomycin. All cell lines tested negative for mycoplasma.

Chemical probes. The chemical probes used in this study were selected based on previously reported studies of photoactivation-dependent proximity labeling and chemical probe relay labeling[38,82]. 3-Ethynyl-4-fluoroaniline (3E-4FA; CAS no. 77123-60-5) was purchased from Leyan.

Plasmid construction. Constructs are described in Supplementary Table 1, and oligonucleotide and siRNA sequences are referenced in Supplementary Table 2. Unless stated otherwise, plasmids were constructed by General Biol. The 12-amino-acid ApbE acceptor sequence GVDGLSGATLTS is referred to throughout as the AAP. The acceptor-site mutant, AAP(T9A), has the sequence GVDGLSGAALTS, in which the threonine at position 9 is replaced by alanine. Histone H2B constructs bearing one to four tandem copies of the AAP were generated to assess the effects of AAP copy number. NUPR1, BANF1 and GNG4 were

Langtaosha (LTS) Preprint doi: https://doi.org/10.65215/LTSpreprints.2026.11.14.000388. This version posted November 14, 2026. The copyright holder for this preprint (which was not certified by peer review) is the author/funder. Creative Commons license: CC Attribution-NonCommercial-NoDerivatives 4.0 https://creativecommons.org/licenses/by-nc-nd/4.0

548 fused to the indicated functional or mutant AAP configurations and epitope tags. Corresponding TurboID
549 fusions were generated for the protein-localization comparisons.

550 Subcellular ApbE targeting used V5–ApbE–3×NLS (nucleus), MITO–V5–ApbE (mitochondria, the
551 mitochondrial matrix targeting sequence derived from the N-terminal 23 amino acids of *COX4*), ERM–V5–
552 ApbE (ER membrane; the ERM-targeting module derives from the 27-amino-acid targeting segment of
553 cytochrome P450 2C1 and places the reporter on the cytosolic face of the ER membrane[83]), V5–ApbE–
554 3×NIK (nucleolus). Compartment-targeted ApbE was paired with the corresponding 2×AAP reporter:
555 H2B–2×AAP (Nuc-2xAAP) for the nucleus, MITO–2×AAP for mitochondria, ERM–2×AAP for the ER
556 membrane and 2×AAP–3×NIK for the nucleolus.

557

558 **Plasmid and siRNA transfection.** Cells were seeded into the indicated culture formats and transfected at
559 approximately 70% confluence using Lipo8000 (Beyotime, C0533). Unless otherwise indicated, plasmid
560 DNA and Lipo8000 were mixed in DMEM, incubated for approximately 10 min at room temperature and
561 added dropwise to cells in fresh complete medium. The medium was replaced after approximately 24 h,
562 and cells were generally analyzed 36–48 h after plasmid transfection.

563 For siRNA-mediated depletion, cells were seeded in antibiotic-free medium and transfected with
564 Lipofectamine RNAiMAX (Thermo Fisher Scientific, 13778150). siRNA and RNAiMAX were diluted
565 separately in Opti-MEM, combined for 20 min at room temperature and added to a final siRNA
566 concentration of approximately 25 nM unless indicated otherwise. Two independent siRNAs per target were
567 used in the BANF1-associated nuclear-envelope assays. In sequential depletion and plasmid-expression
568 experiments, the siRNA transfection preceded plasmid transfection by approximately 24 h. The reported
569 siRNA sequences are referenced in Supplementary Table 2.

570

571 **Stable cell line generation.** Lentiviral particles were produced in HEK293T cells seeded in 6-cm dishes

Langtaosha (LTS) Preprint doi: https://doi.org/10.65215/LTSpreprints.2026.11.14.000388. This version posted November 14, 2026. The copyright holder for this preprint (which was not certified by peer review) is the author/funder. Creative Commons license: CC Attribution-NonCommercial-NoDerivatives 4.0 https://creativecommons.org/licenses/by-nc-nd/4.0

by transfection with 4 μg transfer plasmid, 3 μg psPAX2 and 1 μg pMD2.G using Lipo8000. The medium was exchanged approximately 24 h later. Supernatants were harvested after a further 24 h, passed through a 0.45-μm filter and used to transduce target cells in the presence of 5 μg/ml polybrene. The medium was replaced the following day, and transduced cells were selected using the corresponding antibiotic until stable expression was established.

For compartment-targeted FPPL, HEK293T or HeLa cells expressing the designated ApbE construct were selected with puromycin, generally at 2 μg/ml. Where dual-stable ApbE and AAP reporter lines were generated, puromycin and blasticidin (10 μg/ml, according to cell line and selection stage) were applied. Selection antibiotics were generally omitted during expansion for proteomics experiments.

Expression and purification of recombinant proteins. His-tagged ApbE, MBP–AAP, SUMO–AAP and the indicated AAP(T9A) counterparts were expressed in Escherichia coli BL21(DE3). Individual colonies were inoculated into LB medium containing the appropriate selection antibiotic and cultured at 37 °C with shaking. At an OD_{600} of approximately 0.5, recombinant expression was induced with 0.5 mM IPTG and continued for 7 h at 37 °C. Cells were harvested, resuspended in Tris-based lysis buffer containing protease inhibitors and disrupted by high-pressure homogenization. Lysates were cleared by centrifugation at 4 °C and loaded onto Ni–NTA affinity resin. After washing with imidazole-containing buffer, His-tagged proteins were eluted by increasing the imidazole concentration. Fractions were examined by SDS–PAGE and Coomassie brilliant blue (CBB) staining; protein-containing fractions were pooled, concentrated by centrifugal ultrafiltration, exchanged into Tris–HCl buffer (pH 8.0), quantified, aliquoted and stored at −80 °C.

In vitro ApbE-mediated flavinylation. FMN transfer by ApbE was assayed in Tris–HCl buffer (pH 8.0) containing 1 mM FAD, 1 mM EDTA and 10 mM $MgCl_2$. For the ApbE titration, MBP–AAP was maintained

Langtaosha (LTS) Preprint doi: https://doi.org/10.65215/LTSpreprints.2026.11.14.000388. This version posted November 14, 2026. The copyright holder for this preprint (which was not certified by peer review) is the author/funder. Creative Commons license: CC Attribution-NonCommercial-NoDerivatives 4.0 https://creativecommons.org/licenses/by-nc-nd/4.0

at 15 μM in a 40-μl reaction, and ApbE was added at ApbE: MBP–AAP molar ratios of 0, 0.0625, 0.125, 0.25, 0.5, 1 or 2. Samples were incubated at 30 °C with shaking at 1,050 rpm for 1 h.

For the time course, ApbE and MBP–AAP were each used at 15 μM, and reactions were sampled after 2.5, 5, 10, 20, 40 or 60 min under the same conditions. Reactions were stopped with SDS sample buffer followed by heating. Covalently attached FMN was assessed by in-gel fluorescence using the 488-nm detection channel, with CBB staining used to visualize protein loading. Substrate selectivity was evaluated using SUMO–AAP and MBP–AAP together with their AAP(T9A) counterparts.

In vitro photocatalytic probe screening. SUMO–AAP was first modified with FMN by ApbE under the flavinylation conditions described above for 30 min, placed on ice and purified by chromatography. The resulting SUMO–AAP–FMN was combined with anti-His antibody and each candidate chemical probe at a final probe concentration of 1 mM. Samples were incubated for 1 h at 26 °C with shaking and then illuminated for 10 min. For alkyne probes, labeled proteins were conjugated to azide–rhodamine or azide–biotin by click chemistry for 1 h at 26 °C and analyzed after SDS–PAGE by rhodamine in-gel fluorescence or HRP–streptavidin blotting. FMN installation and total protein input were assessed using 488-nm fluorescence and CBB staining, respectively.

Immunofluorescence analysis of NUPR1 and BANF1 localization. Cells expressing Flag-tagged NUPR1 or BANF1, the corresponding AAP fusion or the TurboID fusion were replated into imaging dishes and fixed with 4% paraformaldehyde. After 0.25% Triton X-100 permeabilization and BSA blocking, Flag was detected using a 488-conjugated Flag-tag recombinant antibody (Proteintech, cat. no. CL488-80010). Nuclei were stained with Hoechst. Images within a given comparison were collected using matched acquisition settings.

For the intensity profiles, Flag and Hoechst fluorescence was sampled along lines crossing

Langtaosha (LTS) Preprint doi: https://doi.org/10.65215/LTSpreprints.2026.11.14.000388. This version posted November 14, 2026. The copyright holder for this preprint (which was not certified by peer review) is the author/funder. Creative Commons license: CC Attribution-NonCommercial-NoDerivatives 4.0 https://creativecommons.org/licenses/by-nc-nd/4.0

individual cells. Flag fluorescence was also quantified from nuclear and cytoplasmic regions of interest, and the nuclear-to-cytoplasmic fluorescence ratio was calculated for each cell. Image measurements were performed in Fiji/ImageJ.

Cellular FPPL labeling. HEK293T cells stably expressing the appropriate compartment-targeted ApbE construct were transfected with the indicated AAP-bearing reporter or protein of interest. Unless specified otherwise, cells were washed with prewarmed Hanks' balanced salt solution (HBSS), incubated in HBSS containing 2 mM 3E-4FA for 1 h at 37 °C and illuminated with 450-nm blue light for 10 min. After illumination, cells were washed with ice-cold PBS and processed for fluorescence microscopy, gel-based analysis or proteomics. Depending on the experiment, controls included AAP(T9A) or other non-flavinylatable variants, an untagged target, probe omission or no illumination.

Cellular probe screening compared the indicated aromatic alkyne analogues. The AAP-, chemical probe- and light-dependence experiments compared H2B–AAP with untagged H2B using 3E-4FA under the indicated conditions. For concentration optimization, nucleus-targeted ApbE was co-expressed with H2B–2×AAP or untagged H2B, and cells were incubated with the indicated concentrations of 3E-4FA before illumination. For wavelength testing, cells were illuminated at 365, 450, 560, 625 or 700 nm or kept in the dark. The indicated AAP sequence variants and H2B fusions containing one to four tandem AAPs were tested in the same general labeling workflow.

In-gel fluorescence and streptavidin detection. Alkyne-modified proteins were conjugated to azide–rhodamine by copper(I)-catalyzed azide–alkyne cycloaddition (CuAAC), separated by SDS–PAGE and visualized by direct rhodamine in-gel fluorescence. For biotin-based assays, click chemistry was performed by adding Biotin-PEG-Azide, freshly prepared TCEP, TBTA and $CuSO_4$ to the reaction mixture, corresponding to final concentrations of 100 μM, 1 mM, 100 μM and 1 mM, respectively. Biotinylated proteins were detected by streptavidin–HRP. AAP-bound FMN was detected in the 488-nm fluorescence channel. The relevant epitope-tag immunoblots and CBB-stained gels were used to assess construct

Langtaosha (LTS) Preprint doi: https://doi.org/10.65215/LTSpreprints.2026.11.14.000388. This version posted November 14, 2026. The copyright holder for this preprint (which was not certified by peer review) is the author/funder. Creative Commons license: CC Attribution-NonCommercial-NoDerivatives 4.0 https://creativecommons.org/licenses/by-nc-nd/4.0

abundance and total protein loading.

Reactive oxygen species perturbation. Cells expressing H2B–2×AAP or the corresponding control were incubated for 1 h in HBSS containing 2 mM 3E-4FA and the indicated modulators of reactive oxygen species (ROS). Unless otherwise specified, additives were 10 mM sodium azide, 100 mM D-mannitol, 5 mM Trolox, 0.5 mM vitamin C or 100 μM H_2O_2; D_2O-containing buffer was used in the singlet-oxygen lifetime experiment. Illuminated samples were exposed to 450-nm blue light for 10 min. Reporter incorporation was examined after rhodamine click conjugation, whereas FMN installation, construct expression and sample loading were assessed by 488-nm in-gel fluorescence, anti-Flag immunoblotting and CBB staining, respectively. These chemical additions were used as mechanistic perturbations rather than as species-specific measurements of an individual ROS.

FPPL sample preparation and LC–MS/MS analysis. BANF1- and GNG4-directed proteomics used HEK293T cells stably expressing nucleus-targeted and cytosol-targeted ApbE, respectively. Cells were grown in 10-cm dishes, with three biological replicates prepared per proteomics condition unless otherwise indicated. After the indicated FPPL labeling procedure, cells were washed with ice-cold PBS containing protease inhibitors, harvested by scraping and lysed by sonication. Lysates were clarified by centrifugation at 4 °C and quantified using a BCA assay (Beyotime, P0009). Protein input was normalized between conditions, with approximately 2 mg total protein used for each sample when sufficient material was available.

Probe-labeled proteins were derivatized by CuAAC using 100 μM biotin–azide, 1 mM tris(2-carboxyethyl) phosphine (TCEP), 100 μM tris(benzyltriazolylmethyl)amine (TBTA) and 1 mM $CuSO_4$. Reactions proceeded for 2 h at 25 °C with shaking. Where indicated, aliquots were retained for streptavidin blotting. Proteins were precipitated by methanol/chloroform extraction, washed with methanol, air-dried

Langtaosha (LTS) Preprint doi: https://doi.org/10.65215/LTSpreprints.2026.11.14.000388. This version posted November 14, 2026. The copyright holder for this preprint (which was not certified by peer review) is the author/funder. Creative Commons license: CC Attribution-NonCommercial-NoDerivatives 4.0 https://creativecommons.org/licenses/by-nc-nd/4.0

669 and dissolved in 8 M urea containing 50 mM ammonium bicarbonate (ABC).

670 Samples were reduced with 10 mM DTT at 55 °C for 40 min, alkylated with 15 mM iodoacetamide
671 for 30 min at room temperature in the dark, and treated with a further 5 mM DTT for 10 min to quench
672 alkylation. After dilution with PBS, biotinylated proteins were enriched using approximately 80 µl
673 prewashed NeutrAvidin agarose (Thermo Fisher Scientific, 29204) for 4 h at room temperature with end-
674 over-end mixing. Beads were washed three times with PBS/0.2% SDS, three times with PBS/1 M urea and
675 twice with PBS.

676 The washed beads were suspended in 300 µl 25 mM ABC containing 1 M urea and 1 mM $CaCl_2$,
677 and 10 µg trypsin was added per sample. On-bead digestion proceeded for approximately 16 h at 37 °C
678 with shaking. Released peptides were recovered, acidified to pH 2–3 with formic acid, desalted on C18
679 material, eluted with 80% acetonitrile, dried under vacuum and reconstituted in 0.1% formic acid for LC–
680 MS/MS.

681 Approximately 500 ng peptide per sample was analyzed using a Q Exactive Plus mass spectrometer
682 with nano-electrospray ionization, controlled by Xcalibur 4.3, coupled to an EASY-nLC 1200 UHPLC.
683 Peptides were separated on a 150-µm-inner-diameter × 20-cm capillary column packed with 1.9-µm C18
684 resin at 300 nl/min. Solvent A was 0.1% formic acid in water and solvent B was 0.1% formic acid in 80%
685 acetonitrile. The gradient increased solvent B from 8% to 50% over 95 min and then to 98% over 6 min.
686 Data-dependent acquisition comprised full MS scans from m/z 350 to 2,000 at a resolution of 120,000
687 (AGC target, 4×10^5; maximum injection time, 150 ms). The ten most intense precursors were selected for
688 HCD with normalized collision energy of 30%, isolation width 1.6 m/z, MS/MS resolution 30,000, AGC
689 target 5×10^4 and maximum injection time 150 ms. The spray voltage was 2.0 kV, the capillary temperature
690 was 320 °C, and the dynamic exclusion time was 30 s. Precursor ions with charges of 1+ or greater than 7+
691 were excluded from MS/MS selection.

692

Langtaosha (LTS) Preprint doi: https://doi.org/10.65215/LTSpreprints.2026.11.14.000388. This version posted November 14, 2026. The copyright holder for this preprint (which was not certified by peer review) is the author/funder. Creative Commons license: CC Attribution-NonCommercial-NoDerivatives 4.0 https://creativecommons.org/licenses/by-nc-nd/4.0

Proteomic data analysis. Raw mass spectrometry files were processed in Proteome Discoverer with a label-free quantification workflow. Exported protein abundance values were analyzed in R. For the BANF1 dataset, proteins showing more than twofold enrichment for BANF1–AAP relative to untagged BANF1 and a reported P value below 0.05 were included in the candidate set. The analogous comparison for GNG4 used functional GNG4–AAP against GNG4–AAP (T9A). Volcano plots display $\log_2$ fold changes against $-\log_{10}$(P values).

Previously reported BANF1 interaction records were retrieved from BioGRID and compared with the BANF1-directed FPPL candidate list; identifiers shared by both lists were counted for the overlap analysis. Reactome and indicated Gene Ontology/pathway annotations were used for functional interpretation. For GNG4, proteins previously implicated in virus-related processes were identified by manual review of database entries and the primary literature and grouped as proviral, antiviral or context-dependent according to their reported effects.

Compartment-specific FPPL proteomics. Compartment-targeted FPPL was performed in HEK293T cells stably expressing the indicated ApbE localization constructs. Cells were transiently transfected with the corresponding 2×AAP reporter: H2B–2×AAP for the nucleus, MITO–2×AAP for mitochondria, ERM–2×AAP for the ER membrane and 2×AAP–3×NIK for the nucleolus. The ERM-targeting module derives from the 27-amino-acid targeting segment of cytochrome P450 2C1 and places the reporter on the cytosolic face of the ER membrane. Following FPPL labeling, samples were processed for CuAAC, NeutrAvidin enrichment, on-bead digestion as detailed above.

Dried peptide samples were dissolved in 10 µL of 0.1% formic acid, and 500 ng of each sample was analyzed using a Thermo Scientific Ultimate 3000 UHPLC system coupled to an Orbitrap Exploris 480 mass spectrometer with a Nanospray Flex ion source. Peptides were loaded onto a 75 µm × 2 cm precolumn (Thermo Fisher Scientific, 164535) and separated on a 75 µm inner-diameter, 25 cm analytical column (Thermo Fisher Scientific, 164941) packed with 2 µm C18 resin. The mobile phases were 0.1% formic acid

Langtaosha (LTS) Preprint doi: https://doi.org/10.65215/LTSpreprints.2026.11.14.000388. This version posted November 14, 2026. The copyright holder for this preprint (which was not certified by peer review) is the author/funder. Creative Commons license: CC Attribution-NonCommercial-NoDerivatives 4.0 https://creativecommons.org/licenses/by-nc-nd/4.0

in water (buffer A) and 0.1% formic acid in 80% acetonitrile (buffer B). Separation was performed at 300 nL/min using a gradient of 10–28% buffer B over 88 min, 30–50% buffer B over 17 min, and 50–99% buffer B over 3 min. Mass spectrometric data were acquired in data-dependent acquisition mode, alternating between full MS1 and MS2 scans. The spray voltage was 2.1 kV, and the ion-transfer capillary temperature was 320 °C. Full MS1 spectra were acquired from m/z 350–1500 at a resolution of 120,000, with an AGC target of 3×10^6 and a maximum injection time of 100 ms. Precursor ions were selected for higher-energy collisional dissociation using a 2 s cycle, a normalized collision energy of 35% and a quadrupole isolation width of 0.7 m/z. MS2 spectra were acquired at a resolution of 30,000, with an AGC target of 2×10^5 and a maximum injection time of 120 ms. Dynamic exclusion was set to 60 s, and ions with charge states of 2+ to 7+ were considered for MS/MS fragmentation.

Proteomic data analysis and ROC analysis. Raw LC–MS/MS data were processed using Proteome Discoverer with label-free quantification. Protein-level $\log_2$ fold changes ($\log_2$FC) and unadjusted P values were exported for downstream analysis. To evaluate compartment specificity, receiver operating characteristic (ROC) analyses were performed independently for Mito–FPPL, ERM–FPPL, and Nuc–FPPL using curated positive and negative reference proteins. For Mito–FPPL, mitochondrial proteins from MitoCarta3.0[52] (n = 1,136) and non-mitochondrial proteins from a published TurboID reference dataset (n = 2,410) were used[25]. For ERM–FPPL, 90 established ERM proteins from a published APEX2 study and 7,421 non-secretory proteins were used as positive and negative references, respectively[40,83]. For Nuc–FPPL, nuclear-only and non-nuclear proteins from OpenCell were used as the corresponding reference sets[50]. Proteins were matched using UniProt accessions, with gene-symbol matching as a fallback for Mito–FPPL. The engineered reporter A0A0871234 was manually assigned as a positive reference for each compartment, and positive assignments took precedence over conflicting negative annotations. Only reference proteins with available quantitative measurements were included in ROC analysis.

ROC curves and areas under the curve (AUCs) were calculated using Python (scikit-learn), with

Langtaosha (LTS) Preprint doi: https://doi.org/10.65215/LTSpreprints.2026.11.14.000388. This version posted November 14, 2026. The copyright holder for this preprint (which was not certified by peer review) is the author/funder. Creative Commons license: CC Attribution-NonCommercial-NoDerivatives 4.0 https://creativecommons.org/licenses/by-nc-nd/4.0

log_2FC as the classification score. Optimal enrichment thresholds were determined by maximizing the Youden index (J = sensitivity + specificity − 1). The resulting AUCs were 0.832, 0.729, and 0.605 for Mito–FPPL, ERM–FPPL, and Nuc–FPPL, respectively, with corresponding log_2FC cutoffs of 0.429, 0.633, and 0.312. Proteins exceeding the respective ROC-derived thresholds and exhibiting an unadjusted $P < 0.05$ were classified as significantly enriched, yielding 424 mitochondrial, 895 ERM-associated, and 953 nuclear FPPL-enriched proteins.

Compartment specificity was further evaluated using independent mitochondrial, secretory-pathway, and nuclear annotations from established protein localization databases. Among the enriched proteins, 286, 617, and 663 were annotated as mitochondrial, secretory-pathway, and nuclear proteins, respectively. Subcellular distributions were characterized using MitoCarta3.0 and GO/STRING annotations.

Fixed-cell visualization of FPPL labeling. Hela cells expressing compartment-targeted ApbE were transiently transfected with the corresponding tagged reporter constructs and subsequently replated into confocal imaging dishes. Cells were washed three times with HBSS, incubated with 3E-4FA for 1 h at 37 °C and illuminated with 450-nm light for 10 min. Following three washes with PBS, cells were fixed with 4% paraformaldehyde for 15 min at room temperature and permeabilized with 0.25% Triton X-100 in PBS for 30 min.

CuAAC was performed on fixed cells for 30 min at room temperature in PBS containing 50 μM Cy3–azide, 1.3 mM BTTAA, 2.5 mM sodium ascorbate and 667 μM $CuSO_4$. Cells were then washed ten times with PBS containing 0.1% Tween-20 (PBST) and blocked with 3% bovine serum albumin (BSA) in PBST for 30 min at room temperature.

For immunofluorescence staining and colocalization analysis, Flag-tagged reporters were detected using a 488-conjugated Flag-tag recombinant antibody (Proteintech, cat. no. CL488-80010) (1:500). Where indicated, cells were incubated overnight at 4 °C with the following primary antibodies: mouse monoclonal

Langtaosha (LTS) Preprint doi: https://doi.org/10.65215/LTSpreprints.2026.11.14.000388. This version posted November 14, 2026. The copyright holder for this preprint (which was not certified by peer review) is the author/funder. Creative Commons license: CC Attribution-NonCommercial-NoDerivatives 4.0 https://creativecommons.org/licenses/by-nc-nd/4.0

anti-V5 (1:500; Cell Signaling Technology, 80076), rabbit monoclonal anti-HSP60 (1:1,000; ABclonal, A0564), rabbit polyclonal anti-calnexin (1:500; Abcam, ab22595) or anti-FBL (1:1,000; Huabio, HA722842). After three washes with PBST, rabbit primary antibodies were detected using Alexa Fluor 647–conjugated goat anti-rabbit secondary antibody (1:500; Beyotime, A0468) for 30 min at room temperature.

Cells were subsequently washed three times with PBST, counterstained with DAPI (Thermo Fisher Scientific, D1306) in PBS for 10 min at room temperature and washed three additional times with PBS. Samples were maintained in PBS during imaging. Confocal fluorescence images were acquired using a ZEISS LSM 980 confocal microscope equipped with ZEN 3.5 software.

FPPL pull-down validation of BANF1-associated proteins. Cells co-expressing nucleus-targeted ApbE and the indicated BANF1 or BANF1–AAP constructs underwent FPPL labeling and biotin–azide conjugation as described above. Biotinylated proteins were isolated on NeutrAvidin beads for 4 h. After washing, retained proteins were eluted directly into SDS loading buffer rather than digested on-bead. Inputs and enriched fractions were probed for SRSF10 and RBMX by immunoblotting.

Co-immunoprecipitation. Cells expressing the indicated bait and candidate proteins were washed twice with ice-cold PBS and lysed in IP buffer containing 1% NP-40, 150 mM NaCl, and 50 mM HEPES (pH 7.6) supplemented with protease inhibitor cocktail. For BANF1 co-immunoprecipitation experiments, cell lysates were additionally treated with nuclease before immunoprecipitation. Lysates were incubated on ice or at 4 °C, clarified by centrifugation, and an aliquot was retained as input. Approximately 1 mg total protein was used for each immunoprecipitation. Lysates were incubated overnight at 4 °C with the indicated bait- or epitope-specific antibody, with species-matched IgG used as a negative control. Pre-washed Protein A/G beads were added and incubated for 1 h at 4 °C. Beads were washed four times with NP-40 lysis buffer and

Langtaosha (LTS) Preprint doi: https://doi.org/10.65215/LTSpreprints.2026.11.14.000388. This version posted November 14, 2026. The copyright holder for this preprint (which was not certified by peer review) is the author/funder. Creative Commons license: CC Attribution-NonCommercial-NoDerivatives 4.0 https://creativecommons.org/licenses/by-nc-nd/4.0

once with RIPA buffer, and bound proteins were eluted in 2× SDS sample buffer by heating.

For GNG4 interaction validation, cells co-expressing GNG4 and the indicated V5-tagged candidate proteins were subjected to immunoprecipitation with anti-GNG4 antibody, followed by immunoblotting for the V5-tagged candidates. For BANF1 interaction validation, epitope-tagged BANF1 and the indicated candidate proteins were analyzed using the same general workflow, with the immunoprecipitation antibody and bait/prey orientation selected according to the corresponding experiment.

Nuclear-envelope reporter assays. RPE-1 reporter cells stably expressing GFP-BANF1, or dual-reporter cells co-expressing GFP-BANF1 and RFP-NLS, were seeded in 12-well plates and transfected with control or candidate-specific siRNAs using RNAiMAX at a final concentration of approximately 25 nM. Cells were replated at low density approximately 24 h after transfection and analyzed by fluorescence microscopy after attachment. Cells containing one or more discrete GFP-BANF1 foci were scored as positive for BANF1 recruitment to nuclear-envelope rupture sites. In dual-reporter experiments, cells showing redistribution of RFP-NLS from the nucleus into the cytoplasm together with GFP-BANF1 foci were scored as positive for nuclear-envelope disruption. Imaging quantifications were performed across three independent biological replicates, with >200 cells quantified per field. Where indicated, two independent siRNAs were tested for each candidate protein.

Lamin A/C and Lamin B1 immunofluorescence. RPE-1 GFP-BANF1 reporter cells were transfected with control or candidate-specific siRNAs at a final concentration of approximately 25 nM. Twenty-four hours after transfection, cells were replated into confocal dishes at low density. Approximately 36 h later, cells were washed with PBS and fixed with 4% paraformaldehyde for 20 min at room temperature. Cells were permeabilized with 0.5% Triton X-100 in PBS for 10 min, washed, and blocked with 3% BSA in PBS for 1 h. Anti-Lamin A/C or anti-Lamin B1 primary antibodies were diluted in 3% BSA/PBS and incubated overnight at 4 °C. Cells were washed with PBS containing 0.05% Triton X-100 and incubated with the corresponding fluorophore-conjugated secondary antibody at 1:1,000 for 1 h at room temperature in the

Langtaosha (LTS) Preprint doi: https://doi.org/10.65215/LTSpreprints.2026.11.14.000388. This version posted November 14, 2026. The copyright holder for this preprint (which was not certified by peer review) is the author/funder. Creative Commons license: CC Attribution-NonCommercial-NoDerivatives 4.0 https://creativecommons.org/licenses/by-nc-nd/4.0

dark. Nuclei were stained with Hoechst for 15 min. Images were acquired using a ZEISS LSM 980 confocal microscope with a 63× objective.

RT–qPCR analysis. Total RNA was isolated using RNAiso Plus/TRIzol and quantified spectrophotometrically. Up to 2 μg RNA was reverse-transcribed with a commercial premix. Quantitative PCR was performed using TB Green/SYBR Green chemistry. A typical 20-μl reaction contained 10 μl 2× master mix, 0.4 μl of each 10 μM primer, approximately 10 ng cDNA and nuclease-free water. Thermal cycling comprised 95 °C for 30 s, followed by 40 cycles of 95 °C for 5 s and 60 °C for approximately 30 s. Transcript levels were normalized to GAPDH or ACTB, as appropriate. Primer sequences are referenced in Supplementary Table 2. This assay was used to evaluate candidate-gene transcript depletion in the BANF1 experiments and to quantify SeV-responsive *IFNB1* and *IFIT1* transcripts after GNG4 or candidate-protein perturbation.

Sendai virus stimulation and GNG4 functional assays. HEK293T cells were used unless otherwise specified. For GNG4 gain-of-function experiments, cells were transfected with a GNG4 expression construct or an empty-vector control. For depletion, cells were transfected with non-targeting siRNA or the indicated independent GNG4-targeting siRNAs. Cells were then challenged with Sendai virus (SeV) for 12 h before harvest unless otherwise stated. For treatments initiated in serum-free medium, serum was restored approximately 1 h after the addition of SeV.

For signaling readouts, cells were washed with ice-cold PBS and lysed in RIPA buffer containing protease and phosphatase inhibitors. SeV-associated signaling was assessed by immunoblotting phosphorylated STAT1 and total STAT1, with actin as a loading reference. For transcriptional readouts, RNA was isolated after SeV challenge and *IFNB1* and *IFIT1* transcripts were quantified by RT–qPCR as described above.

Langtaosha (LTS) Preprint doi: https://doi.org/10.65215/LTSpreprints.2026.11.14.000388. This version posted November 14, 2026. The copyright holder for this preprint (which was not certified by peer review) is the author/funder. Creative Commons license: CC Attribution-NonCommercial-NoDerivatives 4.0 https://creativecommons.org/licenses/by-nc-nd/4.0

Candidate-protein compensation in GNG4-depleted cells. Cells were transfected with control or GNG4-targeting siRNA and, approximately 24 h later, transfected with empty vector or expression plasmids for the indicated FPPL-nominated proteins. After a further approximately 24 h, cells were challenged with SeV for 12 h and then evaluated by phospho-STAT1 immunoblotting or RT–qPCR for *IFNB1* and *IFIT1*.

Western blot analysis. Cells were washed with ice-cold PBS and lysed in PBS or RIPA buffer containing protease inhibitors and, where phosphorylation was assessed, phosphatase inhibitors. Clarified lysates were quantified by BCA assay, and equal protein amounts were denatured in SDS sample buffer, resolved by SDS–PAGE and transferred to PVDF membranes. After blocking, membranes were incubated with the indicated primary antibodies overnight at 4 °C, followed by HRP-conjugated secondary antibodies. Chemiluminescence was used for protein detection; streptavidin–HRP was used for biotin-labeled samples where indicated. Antibody details are referenced in Supplementary Table 3. Band intensities were measured in Fiji/ImageJ where indicated, and phosphorylated STAT1 signals were normalized to total STAT1.

Statistical analysis. All experiments were performed with three biological replicates unless otherwise stated. Statistical analyses were conducted using GraphPad Prism (GraphPad Software) and R and Python. For comparisons between two groups, statistical significance was assessed using a two-sided Student's t-test. For comparisons among three or more groups, one-way analysis of variance (ANOVA) was performed, followed by Tukey's multiple-comparisons test for all pairwise comparisons or Dunnett's multiple-comparisons test for comparisons with a designated control group, as appropriate. Data are presented as mean ± standard deviation (s. d.), unless otherwise stated. For proteomics analyses, only proteins identified in at least two biological replicates were included in subsequent statistical analyses.

Langtaosha (LTS) Preprint doi: https://doi.org/10.65215/LTSpreprints.2026.11.14.000388. This version posted November 14, 2026. The copyright holder for this preprint (which was not certified by peer review) is the author/funder. Creative Commons license: CC Attribution-NonCommercial-NoDerivatives 4.0 https://creativecommons.org/licenses/by-nc-nd/4.0

Data availability

The mass spectrometry data generated in this study have been deposited to the ProteomeXchange Consortium via the iProX[84] partner repository with the dataset identifier PXD087070. Source data are provided with this paper.

References

1 Boix, O. *et al.* pTINCR microprotein promotes epithelial differentiation and suppresses tumor growth through CDC42 SUMOylation and activation. *Nature Communications* **13**, 6840, doi:10.1038/s41467-022-34529-6 (2022).

2 Na, Z. *et al.* Mapping subcellular localizations of unannotated microproteins and alternative proteins with MicroID. *Molecular Cell* **82**, 2900-2911.e2907, doi:https://doi.org/10.1016/j.molcel.2022.06.035 (2022).

3 Zheng, C. *et al.* CRISPR–Cas9-based functional interrogation of unconventional translatome reveals human cancer dependency on cryptic non-canonical open reading frames. *Nature Structural & Molecular Biology* **30**, 1878-1892, doi:10.1038/s41594-023-01117-1 (2023).

4 Deutsch, E. W. *et al.* Expanding the human proteome with microproteins and peptideins. *Nature* **654**, 813-825, doi:10.1038/s41586-026-10459-x (2026).

5 Duffy, E. E. *et al.* Developmental dynamics of RNA translation in the human brain. *Nat Neurosci* **25**, 1353-1365, doi:10.1038/s41593-022-01164-9 (2022).

6 Azam, S., Yang, F. & Wu, X. Finding functional microproteins. *Trends Genet* **41**, 107-118, doi:10.1016/j.tig.2024.12.001 (2025).

7 Mohsen, J. J., Martel, A. A. & Slavoff, S. A. Microproteins-Discovery, structure, and function. *Proteomics* **23**, e2100211, doi:10.1002/pmic.202100211 (2023).

8 Hassel, K. R., Brito-Estrada, O. & Makarewich, C. A. Microproteins: Overlooked regulators of physiology and disease. *iScience* **26**, 106781, doi:10.1016/j.isci.2023.106781 (2023).

9 Schlesinger, D. & Elsasser, S. J. Revisiting sORFs: overcoming challenges to identify and characterize functional microproteins. *FEBS J* **289**, 53-74, doi:10.1111/febs.15769 (2022).

10 Staudt, A. C. & Wenkel, S. Regulation of protein function by 'microProteins'. *EMBO Rep* **12**, 35-42, doi:10.1038/embor.2010.196 (2011).

11 Nah, J. *et al.* Microprotein SMIM26 drives oxidative metabolism via serine-responsive mitochondrial translation. *Mol Cell* **85**, 2759-2775 e2712, doi:10.1016/j.molcel.2025.05.033 (2025).

12 Shi, T. T. *et al.* MAVI1, an endoplasmic reticulum-localized microprotein, suppresses antiviral innate immune response by targeting MAVS on mitochondrion. *Sci Adv* **9**, eadg7053, doi:10.1126/sciadv.adg7053 (2023).

13 Hofman, D. A. *et al.* Translation of non-canonical open reading frames as a cancer cell survival mechanism in childhood medulloblastoma. *Mol Cell* **84**, 261-276 e218, doi:10.1016/j.molcel.2023.12.003 (2024).

14 Nelson, B. R. *et al.* A peptide encoded by a transcript annotated as long noncoding RNA enhances SERCA activity in muscle. *Science* **351**, 271-275, doi:10.1126/science.aad4076 (2016).

Langtaosha (LTS) Preprint doi: https://doi.org/10.65215/LTSpreprints.2026.11.14.000388. This version posted November 14, 2026. The copyright holder for this preprint (which was not certified by peer review) is the author/funder. Creative Commons license: CC Attribution-NonCommercial-NoDerivatives 4.0 https://creativecommons.org/licenses/by-nc-nd/4.0

15 Fisher, M. E. *et al.* Dwarf open reading frame (DWORF) is a direct activator of the sarcoplasmic reticulum calcium pump SERCA. *Elife* **10**, doi:10.7554/eLife.65545 (2021).
16 Stein, C. S. *et al.* Mitoregulin: A lncRNA-Encoded Microprotein that Supports Mitochondrial Supercomplexes and Respiratory Efficiency. *Cell Rep* **23**, 3710-3720 e3718, doi:10.1016/j.celrep.2018.06.002 (2018).
17 Bi, P. *et al.* Control of muscle formation by the fusogenic micropeptide myomixer. *Science* **356**, 323-327, doi:10.1126/science.aam9361 (2017).
18 Koh, M. *et al.* A short ORF-encoded transcriptional regulator. *Proc Natl Acad Sci U S A* **118**, doi:10.1073/pnas.2021943118 (2021).
19 Wacholder, A. *et al.* Community benchmarking and evaluation of human unannotated microprotein detection by mass spectrometry based proteomics. *Nat Commun* **17**, 1241, doi:10.1038/s41467-025-68002-x (2026).
20 Sandmann, C. L. *et al.* Evolutionary origins and interactomes of human, young microproteins and small peptides translated from short open reading frames. *Mol Cell* **83**, 994-1011 e1018, doi:10.1016/j.molcel.2023.01.023 (2023).
21 Qin, W. *et al.* Dynamic mapping of proteome trafficking within and between living cells by TransitID. *Cell* **186**, 3307-3324 e3330, doi:10.1016/j.cell.2023.05.044 (2023).
22 Lee, S. Y. *et al.* Engineered allostery in light-regulated LOV-Turbo enables precise spatiotemporal control of proximity labeling in living cells. *Nat Methods* **20**, 908-917, doi:10.1038/s41592-023-01880-5 (2023).
23 Kim, J. W. *et al.* Molecular recording of calcium signals via calcium-dependent proximity labeling. *Nat Chem Biol* **20**, 894-905, doi:10.1038/s41589-024-01603-7 (2024).
24 Roux, K. J., Kim, D. I., Raida, M. & Burke, B. A promiscuous biotin ligase fusion protein identifies proximal and interacting proteins in mammalian cells. *J Cell Biol* **196**, 801-810, doi:10.1083/jcb.201112098 (2012).
25 Branon, T. C. *et al.* Efficient proximity labeling in living cells and organisms with TurboID. *Nat Biotechnol* **36**, 880-887, doi:10.1038/nbt.4201 (2018).
26 Hung, V. *et al.* Spatially resolved proteomic mapping in living cells with the engineered peroxidase APEX2. *Nat Protoc* **11**, 456-475, doi:10.1038/nprot.2016.018 (2016).
27 Chu, Q. *et al.* Identification of Microprotein-Protein Interactions via APEX Tagging. *Biochemistry* **56**, 3299-3306, doi:10.1021/acs.biochem.7b00265 (2017).
28 Rathore, A. *et al.* MIEF1 Microprotein Regulates Mitochondrial Translation. *Biochemistry* **57**, 5564-5575, doi:10.1021/acs.biochem.8b00726 (2018).
29 Chen, J. *et al.* Application of Twin-Strep Tagging and TurboID Proximity Labeling in Discovery of Microprotein-protein Interactions. *ChemistrySelect* **9**, doi:10.1002/slct.202401782 (2024).
30 Kim, D. I. & Roux, K. J. Filling the Void: Proximity-Based Labeling of Proteins in Living Cells. *Trends Cell Biol* **26**, 804-817, doi:10.1016/j.tcb.2016.09.004 (2016).
31 Ryskina, A. M., Kudriaeva, A. A. & Belogurov Jr, A. A. Microproteins Tracking: When Size Does Really Matter. *Reviews and Advances in Chemistry* **14**, 305-319, doi:10.1134/S2634827624600324 (2024).
32 Fan, X. & Fraaije, M. W. Flavin transferase ApbE: From discovery to applications. *J Biol Chem* **301**, 108453, doi:10.1016/j.jbc.2025.108453 (2025).
33 Bertsova, Y. V. *et al.* Alternative pyrimidine biosynthesis protein ApbE is a flavin transferase catalyzing covalent attachment of FMN to a threonine residue in bacterial flavoproteins. *J Biol Chem* **288**, 14276-14286, doi:10.1074/jbc.M113.455402 (2013).
34 Tong, Y., Lee, M., Drenth, J. & Fraaije, M. W. Flavin-tag: A Facile Method for Site-Specific Labeling of Proteins with a Flavin Fluorophore. *Bioconjug Chem* **32**, 1559-1563, doi:10.1021/acs.bioconjchem.1c00306 (2021).

Langtaosha (LTS) Preprint doi: https://doi.org/10.65215/LTSpreprints.2026.11.14.000388. This version posted November 14, 2026. The copyright holder for this preprint (which was not certified by peer review) is the author/funder. Creative Commons license: CC Attribution-NonCommercial-NoDerivatives 4.0 https://creativecommons.org/licenses/by-nc-nd/4.0

35 Tong, Y., Loonstra, M. R. & Fraaije, M. W. Broadening the Scope of the Flavin-Tag Method by Improving Flavin Incorporation and Incorporating Flavin Analogs. *Chembiochem* **23**, e202200144, doi:10.1002/cbic.202200144 (2022).

36 Bertsova, Y. V., Serebryakova, M. V., Anashkin, V. A., Baykov, A. A. & Bogachev, A. V. Mutational analysis of the flavinylation and binding motifs in two protein targets of the flavin transferase ApbE. *FEMS Microbiol Lett* **366**, doi:10.1093/femsle/fnz252 (2019).

37 Kang, M. G. *et al.* Genetically Encodable Bacterial Flavin Transferase for Fluorogenic Protein Modification in Mammalian Cells. *ACS Synth Biol* **6**, 667-677, doi:10.1021/acssynbio.6b00284 (2017).

38 Zhai, Y. *et al.* Spatiotemporal-resolved protein networks profiling with photoactivation dependent proximity labeling. *Nat Commun* **13**, 4906, doi:10.1038/s41467-022-32689-z (2022).

39 Hananya, N., Ye, X., Koren, S. & Muir, T. W. A genetically encoded photoproximity labeling approach for mapping protein territories. *Proc. Natl Acad. Sci. USA* **120**, e2219339120, doi:10.1073/pnas.2219339120 (2023).

40 Zheng, F., Yu, C., Zhou, X. & Zou, P. Genetically encoded photocatalytic protein labeling enables spatially-resolved profiling of intracellular proteome. *Nat Commun* **14**, 2978, doi:10.1038/s41467-023-38565-8 (2023).

41 Oslund, R. C. *et al.* Detection of cell-cell interactions via photocatalytic cell tagging. *Nat Chem Biol*, doi:10.1038/s41589-022-01044-0 (2022).

42 Lyu, R. *et al.* ASAP-ID: Proximity Labelling With Small Tags. *Mol Cell Proteomics* **25**, 101616, doi:10.1016/j.mcpro.2026.101616 (2026).

43 Kubitz, L. *et al.* Engineering of ultraID, a compact and hyperactive enzyme for proximity-dependent biotinylation in living cells. *Commun Biol* **5**, 657, doi:10.1038/s42003-022-03604-5 (2022).

44 Liu, S. & Costa, M. The role of NUPR1 in response to stress and cancer development. *Toxicol Appl Pharmacol* **454**, 116244, doi:10.1016/j.taap.2022.116244 (2022).

45 Vasseur, S. *et al.* Cloning and expression of the human p8, a nuclear protein with mitogenic activity. *Eur J Biochem* **259**, 670-675, doi:10.1046/j.1432-1327.1999.00092.x (1999).

46 Valacco, M. P. *et al.* Cell growth-dependent subcellular localization of p8. *J Cell Biochem* **97**, 1066-1079, doi:10.1002/jcb.20682 (2006).

47 Lan, W. *et al.* ZZW-115-dependent inhibition of NUPR1 nuclear translocation sensitizes cancer cells to genotoxic agents. *JCI Insight* **5**, doi:10.1172/jci.insight.138117 (2020).

48 Halfmann, C. T. *et al.* Repair of nuclear ruptures requires barrier-to-autointegration factor. *J Cell Biol* **218**, 2136-2149, doi:10.1083/jcb.201901116 (2019).

49 Segura-Totten, M., Kowalski, A. K., Craigie, R. & Wilson, K. L. Barrier-to-autointegration factor: major roles in chromatin decondensation and nuclear assembly. *J Cell Biol* **158**, 475-485, doi:10.1083/jcb.200202019 (2002).

50 Cho, N. H. *et al.* OpenCell: Endogenous tagging for the cartography of human cellular organization. *Science* **375**, eabi6983, doi:10.1126/science.abi6983 (2022).

51 Westberg, M., Holmegaard, L., Pimenta, F. M., Etzerodt, M. & Ogilby, P. R. Rational design of an efficient, genetically encodable, protein-encased singlet oxygen photosensitizer. *J Am Chem Soc* **137**, 1632-1642, doi:10.1021/ja511940j (2015).

52 Rath, S. *et al.* MitoCarta3.0: an updated mitochondrial proteome now with sub-organelle localization and pathway annotations. *Nucleic Acids Res* **49**, D1541-D1547, doi:10.1093/nar/gkaa1011 (2021).

53 Prissette, M. *et al.* Disruption of nuclear envelope integrity as a possible initiating event in tauopathies. *Cell Rep* **40**, 111249, doi:10.1016/j.celrep.2022.111249 (2022).

Langtaosha (LTS) Preprint doi: https://doi.org/10.65215/LTSpreprints.2026.11.14.000388. This version posted November 14, 2026. The copyright holder for this preprint (which was not certified by peer review) is the author/funder. Creative Commons license: CC Attribution-NonCommercial-NoDerivatives 4.0 https://creativecommons.org/licenses/by-nc-nd/4.0

54 Kono, Y. *et al.* Nucleoplasmic lamin C rapidly accumulates at sites of nuclear envelope rupture with BAF and cGAS. *J Cell Biol* **221**, doi:10.1083/jcb.202201024 (2022).
55 Janssen, A. *et al.* The BAF A12T mutation disrupts lamin A/C interaction, impairing robust repair of nuclear envelope ruptures in Nestor-Guillermo progeria syndrome cells. *Nucleic Acids Res* **50**, 9260-9278, doi:10.1093/nar/gkac726 (2022).
56 Horikoshi, N. *et al.* Cryo-EM structures of the BAF-Lamin A/C complex bound to nucleosomes. *Nat Commun* **16**, 1495, doi:10.1038/s41467-025-56823-9 (2025).
57 Oughtred, R. *et al.* The BioGRID database: A comprehensive biomedical resource of curated protein, genetic, and chemical interactions. *Protein Sci* **30**, 187-200, doi:10.1002/pro.3978 (2021).
58 Ye, G. *et al.* Mitotic DNA repair by TMEJ suppresses replication stress-induced nuclear envelope reassembly defect. *Nat Commun* **16**, 8836, doi:10.1038/s41467-025-63942-w (2025).
59 Kankanamge, D., Tennakoon, M., Karunarathne, A. & Gautam, N. G protein gamma subunit, a hidden master regulator of GPCR signaling. *J Biol Chem* **298**, 102618, doi:10.1016/j.jbc.2022.102618 (2022).
60 Han, C. *et al.* Voltage-Dependent Anion Channel 1 Interacts with Ribonucleoprotein Complexes To Enhance Infectious Bursal Disease Virus Polymerase Activity. *J Virol* **91**, doi:10.1128/JVI.00584-17 (2017).
61 Harel, S. *et al.* Analysis of individual HIV-1 budding event using fast AFM reveals a multiplexed role for VPS4. *Biophys J* **121**, 4229-4238, doi:10.1016/j.bpj.2022.08.035 (2022).
62 Barouch-Bentov, R. *et al.* Hepatitis C Virus Proteins Interact with the Endosomal Sorting Complex Required for Transport (ESCRT) Machinery via Ubiquitination To Facilitate Viral Envelopment. *mBio* **7**, doi:10.1128/mBio.01456-16 (2016).
63 Acharya, D. *et al.* Actin cytoskeleton remodeling primes RIG-I-like receptor activation. *Cell* **185**, 3588-3602 e3521, doi:10.1016/j.cell.2022.08.011 (2022).
64 Wang, L. *et al.* Sec8: a novel positive regulator of RIG-I in anti-RNA viral defense. *Cell Death Dis* **17**, 165, doi:10.1038/s41419-026-08414-9 (2026).
65 Wang, L. *et al.* Unveiling EXOC4/SEC8: a key player in enhancing antiviral immunity by inhibiting the FBXL19-STING1-SQSTM1 signaling axis. *Autophagy* **21**, 2578-2596, doi:10.1080/15548627.2025.2511077 (2025).
66 Wu, J. *et al.* SARS-CoV-2 ORF9b inhibits RIG-I-MAVS antiviral signaling by interrupting K63-linked ubiquitination of NEMO. *Cell Rep* **34**, 108761, doi:10.1016/j.celrep.2021.108761 (2021).
67 Ulupinar, P., Caglayan, E., Rayaman, E., Nagata, K. & Turan, K. The mitochondrial carrier homolog 2 is involved in down-regulation of influenza A virus replication. *Mol Biol Rep* **51**, 642, doi:10.1007/s11033-024-09584-5 (2024).
68 Zhou, Y. Q. *et al.* SARS-CoV-2 pseudovirus enters the host cells through spike protein-CD147 in an Arf6-dependent manner. *Emerg Microbes Infect* **11**, 1135-1144, doi:10.1080/22221751.2022.2059403 (2022).
69 Marchant, D. *et al.* ERK MAP kinase-activated Arf6 trafficking directs coxsackievirus type B3 into an unproductive compartment during virus host-cell entry. *J Gen Virol* **90**, 854-862, doi:10.1099/vir.0.005868-0 (2009).
70 Karttunen, H. *et al.* Co-opting the Fanconi anemia genomic stability pathway enables herpesvirus DNA synthesis and productive growth. *Mol Cell* **55**, 111-122, doi:10.1016/j.molcel.2014.05.020 (2014).
71 Hoskins, E. E. *et al.* The fanconi anemia pathway limits human papillomavirus replication. *J Virol* **86**, 8131-8138, doi:10.1128/JVI.00408-12 (2012).

Langtaosha (LTS) Preprint doi: https://doi.org/10.65215/LTSpreprints.2026.11.14.000388. This version posted November 14, 2026. The copyright holder for this preprint (which was not certified by peer review) is the author/funder. Creative Commons license: CC Attribution-NonCommercial-NoDerivatives 4.0 https://creativecommons.org/licenses/by-nc-nd/4.0

72 Kofler, N. *et al.* The Rab-effector protein RABEP2 regulates endosomal trafficking to mediate vascular endothelial growth factor receptor-2 (VEGFR2)-dependent signaling. *J Biol Chem* **293**, 4805-4817, doi:10.1074/jbc.M117.812172 (2018).

73 Strahle, L. *et al.* Activation of the beta interferon promoter by unnatural Sendai virus infection requires RIG-I and is inhibited by viral C proteins. *J Virol* **81**, 12227-12237, doi:10.1128/JVI.01300-07 (2007).

74 Shi, Y. *et al.* Decoding microprotein interactome via a minimal genetically encoded photocatalytic proximity labeling system. *Nature Communications*, doi:10.1038/s41467-026-78409-9 (2026).

75 Zhou, W. *et al.* FlAsH-ID enables live-cell photoproximity labeling with a short peptide tag. *Nat Chem Biol*, doi:10.1038/s41589-026-02366-z (2026).

76 Adams, S. R. *et al.* New biarsenical ligands and tetracysteine motifs for protein labeling in vitro and in vivo: synthesis and biological applications. *J Am Chem Soc* **124**, 6063-6076, doi:10.1021/ja017687n (2002).

77 Halo, T. L., Appelbaum, J., Hobert, E. M., Balkin, D. M. & Schepartz, A. Selective recognition of protein tetraserine motifs with a cell-permeable, pro-fluorescent bis-boronic acid. *J Am Chem Soc* **131**, 438-439, doi:10.1021/ja807872s (2009).

78 Martin, B. R., Giepmans, B. N., Adams, S. R. & Tsien, R. Y. Mammalian cell-based optimization of the biarsenical-binding tetracysteine motif for improved fluorescence and affinity. *Nat Biotechnol* **23**, 1308-1314, doi:10.1038/nbt1136 (2005).

79 Stroffekova, K., Proenza, C. & Beam, K. G. The protein-labeling reagent FLASH-EDT2 binds not only to CCXXCC motifs but also non-specifically to endogenous cysteine-rich proteins. *Pflugers Arch* **442**, 859-866, doi:10.1007/s004240100619 (2001).

80 Langhorst, M. F., Genisyuerek, S. & Stuermer, C. A. Accumulation of FlAsH/Lumio Green in active mitochondria can be reversed by beta-mercaptoethanol for specific staining of tetracysteine-tagged proteins. *Histochem Cell Biol* **125**, 743-747, doi:10.1007/s00418-005-0136-3 (2006).

81 Gaietta, G. M. *et al.* Golgi twins in late mitosis revealed by genetically encoded tags for live cell imaging and correlated electron microscopy. *Proc Natl Acad Sci U S A* **103**, 17777-17782, doi:10.1073/pnas.0608509103 (2006).

82 Zhai, Y. *et al.* Global profiling of functional histidines in live cells using small-molecule photosensitizer and chemical probe relay labelling. *Nat Chem* **16**, 1546-1557, doi:10.1038/s41557-024-01545-6 (2024).

83 Hung, V. *et al.* Proteomic mapping of cytosol-facing outer mitochondrial and ER membranes in living human cells by proximity biotinylation. *Elife* **6**, doi:10.7554/eLife.24463 (2017).

84 Ma, J. *et al.* iProX: an integrated proteome resource. *Nucleic Acids Res* **47**, D1211-D1217, doi:10.1093/nar/gky869 (2019).

Acknowledgements

We thank the mass spectrometry, imaging and sequencing core facility in Shenzhen Bay Laboratory for their assistance in running samples and collecting data. This work was supported by Guangdong Special Support Plan for Outstanding Young Talents (2023TQ07A238 to G.L.), Youth Science Fund Program (Category B) of the National Natural Science Foundation of China (No. 22522703 to G. Li), the National

Langtaosha (LTS) Preprint doi: https://doi.org/10.65215/LTSpreprints.2026.11.14.000388. This version posted November 14, 2026. The copyright holder for this preprint (which was not certified by peer review) is the author/funder. Creative Commons license: CC Attribution-NonCommercial-NoDerivatives 4.0 https://creativecommons.org/licenses/by-nc-nd/4.0

Natural Science Foundation of China (Young Scientists Fund, 32501321 to Z. Fang), and the China Postdoctoral Science Foundation (2024M762153 to Z. Fang).

Author contributions

G.L. conceived the project and supervised the research. Z.F. and G.L. designed the study and analyzed the data. Z.F., X.Z. and C.B. contributed to experimental design, method development, data analysis and manuscript preparation. M.G. and K.L. contributed to experimental implementation and validation. Y.H. and L.D. provided guidance and supervision for the BANF1 proximity-interactome studies and nuclear-envelope rupture assays. X.Y. developed Python scripts for proteomic data processing, statistical analysis and data visualization. Z.F. and G.L. wrote the manuscript with input from all authors. All authors reviewed and approved the final manuscript.